ISPRS Journal of Photogrammetry and Remote Sensing 189 (2022) 1–22

Contents lists available at ScienceDirect

ISPRS Journal of Photogrammetry and Remote Sensing

journal homepage: www.elsevier.com/locate/isprsjprs

Nation-wide mapping and classification of ground deformation phenomena through the spatial clustering of P-SBAS InSAR measurements: Italy case study

Davide Festa [a,*], Manuela Bonano [b], Nicola Casagli [a,c], Pierluigi Confuorto [a], Claudio De Luca [b], Matteo Del Soldato [a], Riccardo Lanari [b], Ping Lu [d], Michele Manunta [b], Mariarosaria Manzo [b], Giovanni Onorato [b], Federico Raspini [a], Ivana Zinno [b], Francesco Casu [b]

[a] Department of Earth Sciences, University of Firenze, Via La Pira 4, Firenze, Italy
[b] IREA-CNR, Via Diocleziano 328, Napoli - via Bassini 15, Milano, Italy
[c] National Institute of Oceanography and Applied Geophysics - OGS, Borgo Grotta Gigante n. 42/c, Sgonico (Trieste), Italy
[d] College of Surveying and Geo-Informatics, Tongji University, Siping Road 1239, Shanghai, China

ARTICLE INFO

Keywords:
Mapping
National scale
Semi-automatic classification
Ground displacement
Deformation map DInSAR

ABSTRACT

The rising availability of satellite-based multi-temporal interferometric datasets covering large areas of the Earth surface constitutes a huge asset in the context of operational workflows aimed at improving land risk assessment and management. In order to cost-effectively handle huge amount of data, we design a semi-automatic procedure to quickly identify, map and inventory ground and infrastructures displacements by means of spatial clustering performed over very large-scale Differential Synthetic Aperture Radar Interferometry (DInSAR) datasets. The detected deforming areas are then evaluated against the Line of Sight (LOS) velocity vector decomposition and the accessible ancillary layers for a preliminary classification of the triggering factors. We apply our methodology to the mean ascending and descending deformation maps covering the whole Italian territory resulting from 3294 and 2868 Sentinel-1 (S1) acquisitions respectively, spanning from March 2015 to December 2018 and processed through the Parallel Small BAseline Subset (P-SBAS) technique. By setting a displacement rate threshold of ± 1 cm/year, a total number of 14,638 areas resulting from both geometries are found to suffer from instability phenomena, the origin of which are in turn preliminary sorted in 11 classes split between natural causes and man-made activities. With 2 degrees of confidence, we classified landslide and subsidence events as the main causes of deformation within the Italian territory, constituting respectively 31% and 27% of the total unstable areas, followed by volcanic-related processes (22%). Lastly, we provide a complete overview of the deformation phenomena which have recently occurred on the Italian Peninsula starting from national scale statistical analysis and ending up with local scale investigations according to the deformation patterns visible through the vertical and East-West components of motion.

1. Introduction

Differential Synthetic Aperture Radar (SAR) Interferometry (DInSAR) is a well-known remote sensing technique which allows the generation of spatially dense deformation maps by comparing the phase of successive radar images of the same target area (Gabriel et al., 1989). Since the '90 s (Massonnet et al., 1993) satellite Differential SAR Interferometry has been exploited by the scientific community to detect and map surface displacements due to geological hazardous events such as landslides (Calò et al., 2014; Rosi et al., 2017; Solari et al., 2020) land subsidence (Bianchini et al., 2018; Ezquerro et al., 2020; Osmanoğlu et al., 2011), volcanic and tectonic-related surface deformations (De Novellis et al., 2019; Kobayashi et al., 2015; Lanari et al., 2002; Lundgren and Rosen 2003; Tizzani et al., 2013). The last years have seen the interferometry technique to impose itself as a global monitoring tool suited for the near real-time mitigation against the impact of natural hazards and anthropogenic sources of ground motion. This can be ascribed to (*i*) the enhanced capabilities of the recent satellites systems,

* Corresponding author at: Dipartimento di Scienze della Terra, Università degli Studi di Firenze, Via La Pira, 4, 50121 Florence, Italy.
E-mail address: davide.festa@unifi.it (D. Festa).

https://doi.org/10.1016/j.isprsjprs.2022.04.022
Received 16 December 2021; Received in revised form 12 April 2022; Accepted 22 April 2022
Available online 6 May 2022

which are able to provide unprecedent amounts of interferometric data with increasing satellite revisit frequency; *(ii)* the availability of data archives with a free and open access policy; (*iii*) the development of efficient algorithms aimed at optimizing the DInSAR processing chain for the wide spatial scale analysis.

In this context, a key role has been played by the launch of Copernicus Sentinel-1A and Sentinel-1B satellites in April 2014 and April 2016, respectively. Developed within the Copernicus program (https://www.copernicus.eu/en) and primarily devoted to ground deformation monitoring, the S1 constellation is equipped with C-band sensors and offers an unprecedent revisiting time down to 6 days (12 days when exploiting one satellite only). The key element of S1 constellation is its main acquisition mode on land, referred to as Interferometric Wide Swath (IWS), which implements the Terrain Observation by Progressive Scans (TOPS) technique (De Zan and Guarnieri, 2006). Moreover, the S1 data benefit from a worldwide coverage, systematic acquisition plan, rapid product delivery, and a free data policy (Torres et al., 2012).

About DInSAR algorithms, the Small BAseline Subset (SBAS, Berardino et al., 2002; Lanari et al., 2004) technique and in particular its parallel computing version (P-SBAS, Casu et al., 2014; Manunta et al., 2019; Zinno et al., 2015), implements a complete advanced DInSAR processing scheme which ends with the generation of the Line of Sight (LOS) deformation time series and corresponding mean deformation velocity maps. P-SBAS exploits interferograms characterized by small temporal and/or spatial baselines between the acquisition orbits, in order to mitigate the decorrelation phenomena and consequently reduce possible phase unwrapping errors (Fornaro et al., 1997a; Fornaro et al., 1997b), and relies on the use of High-Performance Computing (HPC) facilities, as those available through Cloud Computing (CC) infrastructures. The combined use of the S1 system peculiarities, the P-SBAS processing chain efficiency and the large availability of computing resources provided by CC infrastructures makes feasible surface deformations mapping in deferred time and/or routine displacement monitoring with a sub-centimeter accuracy at national scale and in limited time frame (Manunta et al., 2019; Zinno et al., 2018).

These peculiarities represent a big revolution in the Earth Observation scenario, in terms of operational capability and amount of radar involved. In this context, some relevant efforts in the direction of extensive exploitation of large SAR archives has already been carried out at a various scale of analysis, such as regional (Bonì et al., 2020; Kalia 2018; Solari et al., 2019), nation-wide (Dehls et al., 2019; Di Martire et al., 2017; Kalia et al., 2017; Morishita et al., 2020; Zinno et al., 2018), or continental (Crosetto et al., 2020; Lanari et al., 2020). Moreover, an important Copernicus initiative named the European Ground Motion Service (EGMS, Crosetto et al., 2020) will provide, for the next three years, ground deformation products over Europe with a one year-update plan, thus representing an unprecedented amount of freely accessible DInSAR results.

The extraction and characterization of ground motion areas from deformation maps is a time-consuming task in any DInSAR-based analysis, especially when large and geologically complex areas are investigated. Given the large number of Measurement Points (MPs) which can be generated independently of the specific processing approach adopted, the compelling need for adopting automatic strategies to handle large volumes of data is nowadays crucial. Along the processing chain, new post-processing algorithms urge to be developed in order to maximize the value-added products from the increasing availability of interferometric results. In particular, they should be devoted to: (*i*) filtering regional-scale DInSAR products to identify the most potentially hazardous motions; (*ii*) automatically determining the magnitude and the type of deformation; (*iii*) obtaining a preliminary assessment of the underlying processes that triggered the detected areas affected by deformation (which could be further analyzed and on-field validated). So far, the extraction of moving areas relied on simple and reproducible methods, such as hot-spot-like approaches (Barra et al., 2017; Bianchini et al., 2012; Lu et al., 2012; Meisina et al., 2008) or methods based on clustering analysis (Montalti et al., 2019; Solari et al., 2019; Tomás et al., 2019) applied at basin or region scale. The final output is a geodatabase containing multiple information, regarding both magnitudes of ground motions and the underlying triggering process.

In this paper, we present the results of a post-processing analysis carried out by means of spatial clustering analyses on P-SBAS data (with a ground pixel size of about 80 × 80 m) covering the whole Italian territory over both ascending and descending orbits (Manzo et al., 2019). The whole S1 archive acquired from March 2015 to December 2018 is fully exploited in order to identify the ground deformation phenomena which have been recently affecting the Italian peninsula. By means of semi-automatic GIS (Geographic Information Systems) models specifically designed for the purpose, the detected active MPs have been characterized and aggregated in polygonal clusters, hereinafter defined as Moving Area Clusters (MAC), which were then classified inferring the motion trigger primarily by evaluating the intersection with freely accessible ancillary data and preexisting geo-hazards inventory maps and, secondarily, through the analysis of the 2D decomposition of LOS displacements. Statistical evaluations have been performed and site-specific ground deformation processes have been further analyzed and displayed, in order to provide a comprehensive view of the surface deformation events occurred in Italy between March 2015 and December 2018.

To the best of our knowledge, this is the first example of a nation-wide surface displacement mapping where the retrieved clustered areas are classified in a semi-automatic way. Being Italy a country exposed to a large number of natural hazards, from volcanic eruptions and earthquakes to landslides and subsidence, which are often concurrent in time and space, the “radar interpretation” (Farina et al., 2007) concerning thousands of active motion areas has to be as automated as possible. As suggested by Tomás et al. (2019), the adopted classification algorithm follows a simple approach and relies on few input data (*i.e.*, the DInSAR dataset itself and generally open-access ancillary data) and is able to realize a preliminary screening of both natural and man-induced phenomena which lead to surface deformations during the monitoring period.

The detection and characterization of the deformation processes affecting the Earth surface constitute a milestone for what concerns the correct management and mitigation of their impact on both vulnerable population and infrastructures. Therefore, the implementation of relatively simple DInSAR-based solutions, in the context of wide areas monitoring, should constitute a necessary step towards the modernisation and maximization of the resources available to stakeholders involved in territorial planning and civil protection.

2. Data and methods

The presented methodology relies on a complete multi-scale approach starting from a country-wide mosaicked mean deformation velocity map and ending up with a classified active motion areas database. Results are then presented and discussed through site-specific, detailed scale analysis (Fig. 1). The methodological approach consists of three post-processing phases performed over the P-SBAS outcomes resulting from S1 IWS archives: (*i*) semi-automatic spatial clustering of active ground deformation areas affecting the Italian territory, thus identifying the MACs; (*ii*) subsequent automatic classification by means of superimposition on pre-existing inventories, thematic maps and by LOS velocity vector decomposition for every MAC; (*iii*) local scale analysis and characterization of the detected ground deformation processes through the investigation of the deformation pattern.

2.1. Input datasets

2.1.1. Nation-wide P-SBAS results from Sentinel-1 IWS archives

The DInSAR deformation map covering the whole Italian territory

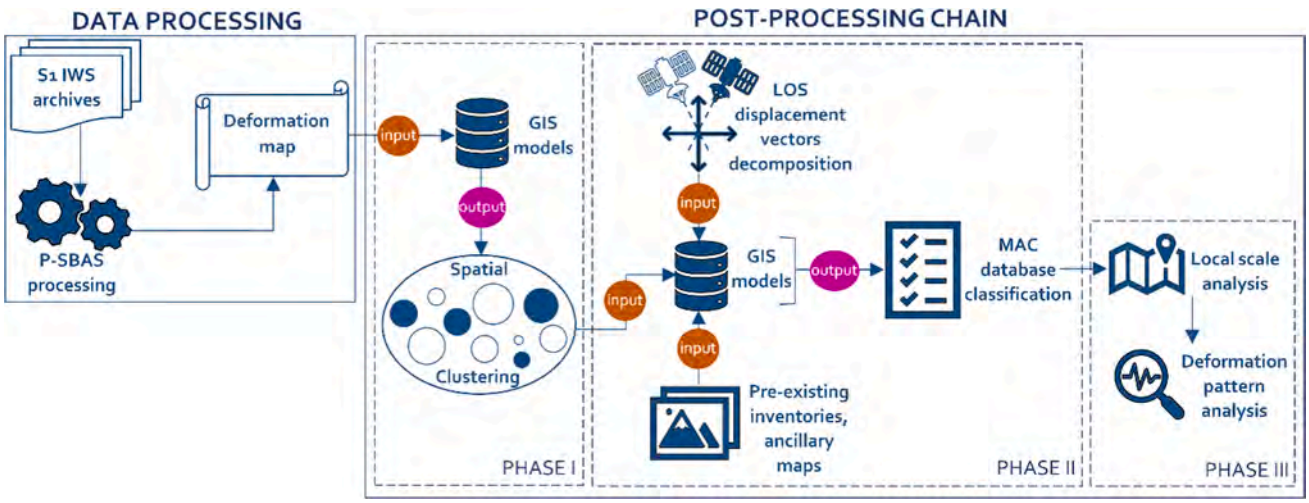

Fig. 1. Flow chart of the adopted methodology.

represents the starting point of the MAC generation. Such a DInSAR deformation map covers an area of more than 300,000 km^2 and it has been computed within a project lead by the Italian Ministry of Economic Development aimed at investigating the deformation phenomena affecting the Italian territory (Manzo et al., 2019). The realization of the mean deformation velocity map relies on interferometric analysis at national scale obtained through an efficient SBAS processing chain, namely P-SBAS (Casu et al., 2014), which simultaneously exploits a fast access to the S1 data archives, High-Performance Computing resources and external geodetic data (De Luca et al., 2021; Manunta et al., 2019; Zinno et al., 2018). In particular, the P-SBAS processing chain takes full advantage from the peculiarities of the S1 IWS acquisitions mode, where every acquisition strip is composed of several swaths and bursts. This data partitioning promotes the distribution of the S1 interferometric processing of the independent bursts on a large number of different computing nodes or CPUs. Moreover, the S1 constellation, being characterized by a very small orbital tube (with a nominal diameter of about 200 m), makes the derived raw data particularly suitable to be processed through the P-SBAS approach resulting in a minimized spatial decorrelation. Having in mind fast processing of huge volumes of S1 data, the Cloud Computing environments are perfectly appropriate for fast processing of huge volumes of S1 data, leveraging on storage capability, large variety of instances for the computation and resources scalability with respect to the amount of data to be processed.

In this work, Sentinel-1A and 1B radar images acquired in C-band (wavelength 5.5 cm and incidence angle ranging from 33° to 43°) are exploited in ascending and descending orbits covering the whole Italian territory (Fig. 2). The overall investigated area has been divided into 19 and 17 frames, from 5 and 6 ascending and descending orbit tracks, respectively, with an average size of almost 200 km × 250 km (azimuth and range). An overlap between frames has been preserved, covering almost 20% of the frame size for two subsequent ones in the azimuth direction, thus guaranteeing an additional consistency check for the continuity preservation of the achieved results (Fig. 2).

The retrieved DInSAR products (Fig. 3) have been obtained by using data acquired from March 2015 to December 2018 with a resulting pixel dimension of about 80 m × 80 m (Table 1). The DInSAR processing has been carried out following the S1 P-SBAS approach (Manunta et al., 2019), which includes appropriate interferogram phase filtering (De Luca et al., 2021; Pepe et al., 2015) and accurate phase unwrapping procedures (Pepe and Lanari 2006). Atmospheric phase screen and possible residual phase artifacts are filtered out by also exploiting global navigation satellite system (GNSS) position time series, which in turn are properly selected for the sufficient extension in time and for not being affected by local displacement effects, as detailed in Lanari et al., 2020. The final average DInSAR measurement accuracy is of about 5 mm on the single retrieved displacement time series (Manunta et al., 2019). In order to produce high-precision DInSAR measurements, only pixels holding a temporal coherence (Pepe and Lanari 2006) value greater than 0.9 were retained for this work. Taking into account both ascending and descending DInSAR nation-wide datasets, a total of 15,247,842 MPs have been made available for this research (Table 1).

2.1.2. *Pre-existing inventories and ancillary data layers*

The joint use of geohazard-related inventories and ancillary maps is crucial for the classification and characterization of the DInSAR-based MAC database. In this work, both pre-existing freely accessible informative layers and re-elaborated products were employed. They can be summarized in three categories, pre-existing geohazard inventories, ancillary maps, slope maps, here resumed:

- The selected pre-existing inventories are related to different geohazards, namely landslides, earthquake-induced landslides and subsidence. In the first case, the Italian Landslide Inventory (IFFI project) at 1:10 000 scale has been chosen since it depicts the spatial distribution of past and present mass movements within Italy (represented as polygons or points). Moreover, the Italian Catalogue of Earthquake-induced ground failures in Italy (Fortunato et al., 2012) supplies a detailed picture of the ground effects due to the seismic sequence occurred on 2016–2017 in the Central Apennines (Improta et al., 2019; Martino 2017) and it is therefore used as a proxy to extrapolate spatially coincident earthquake-related moving areas. Finally, a subsidence inventory map has been derived based on the analysis conducted by Solari et al. (2018), who spatially defined subsidence areas in Italy monitored by means of interferometric techniques in the last 20 years;
- Ancillary maps consist of thematic layers such as land use, physiographic and lithological maps. In particular, the following layers have been deployed: CORINE Land Cover map at 1:100 000 scale from the Copernicus Land Monitoring Service and updated for the 2018 reference year, where up to 44 classes of land covers are distinguished; *Carta della Natura* map at 1:250 000 scale (Amadei et al., 2003) provided by ISPRA where the Italian peninsula is subdivided into 37 different physiographic units associated to geographically defined sections of the territory; 1:500,000 lithological map of Italy with 16 associated different classes (https://www.isprambiente.gov.it/images/progetti/progetto-1250-ita.jpg);
- The slope map (raster format) of Italy has been computed from the TINITALY/01 DEM, a digital elevation model with 10 m-cell sizes covering the whole Italy territory (Tarquini et al., 2012).

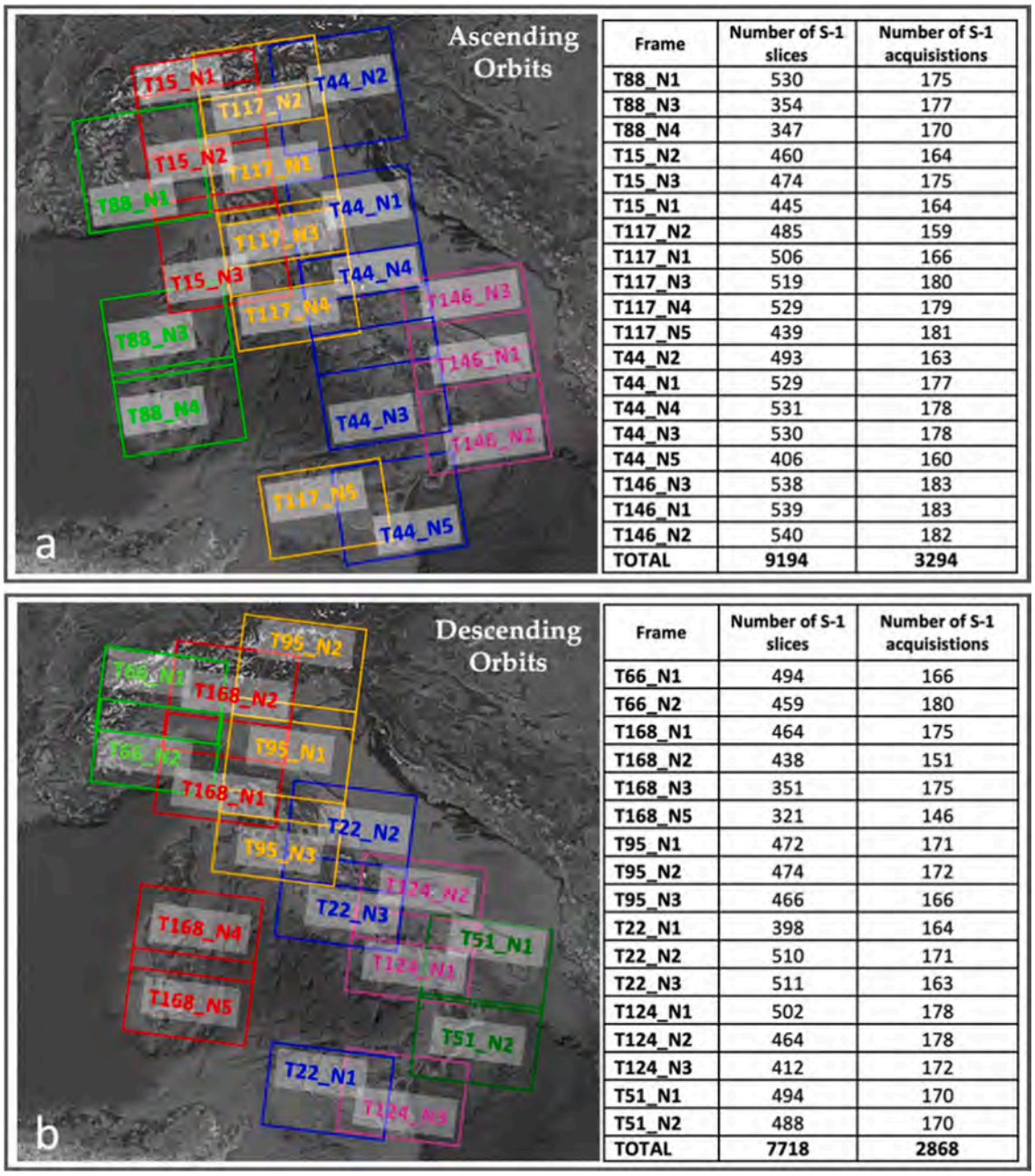

Frame	Number of S-1 slices	Number of S-1 acquisistions
T88_N1	530	175
T88_N3	354	177
T88_N4	347	170
T15_N2	460	164
T15_N3	474	175
T15_N1	445	164
T117_N2	485	159
T117_N1	506	166
T117_N3	519	180
T117_N4	529	179
T117_N5	439	181
T44_N2	493	163
T44_N1	529	177
T44_N4	531	178
T44_N3	530	178
T44_N5	406	160
T146_N3	538	183
T146_N1	539	183
T146_N2	540	182
TOTAL	9194	3294

Frame	Number of S-1 slices	Number of S-1 acquisistions
T66_N1	494	166
T66_N2	459	180
T168_N1	464	175
T168_N2	438	151
T168_N3	351	175
T168_N5	321	146
T95_N1	472	171
T95_N2	474	172
T95_N3	466	166
T22_N1	398	164
T22_N2	510	171
T22_N3	511	163
T124_N1	502	178
T124_N2	464	178
T124_N3	412	172
T51_N1	494	170
T51_N2	488	170
TOTAL	7718	2868

Fig. 2. Optical image of the Italian territory with superimposed the representation of the processed S1 frames within the S1 IWS P-SBAS processing chain. (a)-(b) represent the processed frames over ascending and descending orbits, respectively. On the right side of the picture details about the processed slices and the corresponding acquisitions for each frame are shown. Note that each color in (a) and (b) identifies a different track.

2.2. Post-processing chain

2.2.1. Spatial clustering

Groups of spatial objects with similar features can be merged together into clusters. Spatial clustering analysis is particularly useful when it is applied to filter nation-wide DInSAR databases and retain MPs representative of relatively large average displacement behavior, in order to detect the most potentially active hazardous motions.

The setup of an automatic GIS model, consisting in a completely reproducible sequence of geoprocessing tools, allowed the filtering, the extraction and the spatial aggregations of MPs into clusters of moving areas with a significant displacement rate. The model workflow consists of a chain of tasks connected together where the output of every process is fed into another process. In particular, 10 different built-in GIS tools were exploited while, besides the need for specifying the input data file and the working folder, only 3 parameters are requested to be set to make the model run. The characteristics of the final output strongly depend on the model parameters settings which can be described as follows:

- Displacement rate threshold, whose function is to filter out stable MPs (*i.e.* ground pixels holding absolute velocity values lower than the chosen threshold);
- Buffer size, which is the MP radius of "influence" that should be set in accordance with the spatial resolution of the DInSAR dataset (e.g., if the distance between two MPs is greater than double the radius they are not aggregated in the same cluster);

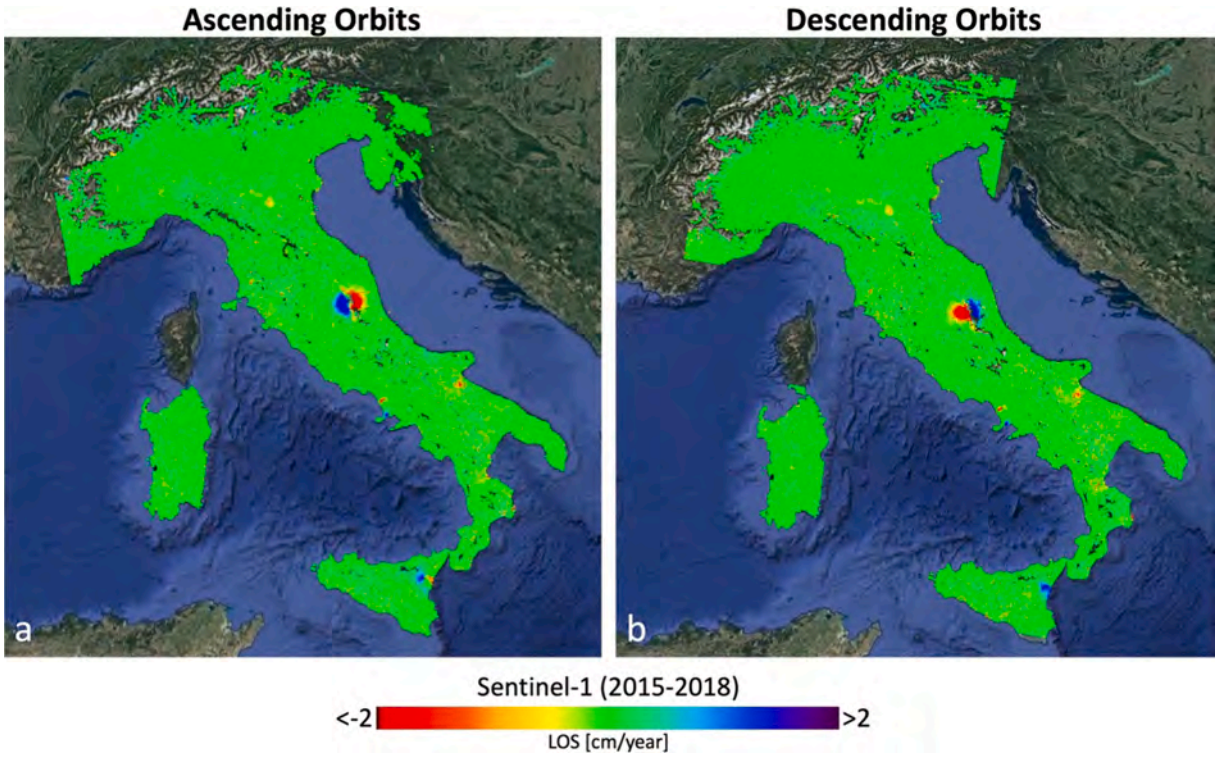

Fig. 3. Ascending and descending nation-wide P-SBAS deformation velocity maps obtained from the exploitation of the whole S1 IWS archive spanning the March 2015 – December 2018 time interval.

Table 1
Features of the input ascending and descending DInSAR datasets, including the MPs (Measurement Points) count, the smallest and largest values of velocities encountered, the standard deviation of the velocity distribution and the number of MPs per km2.

Satellite (orbit)	Time interval (*Number of images*)	MPs Count	Vel. min – max (cm/yr)	Vel. Std. deviation	MP Density (num./km^2)
Sentinel-1 (ascending)	23 Mar 2015 – 26 Dec 2018 (*3,294*)	8,066,243	−10.1 – 6.8	0.3	27.7
Sentinel-1 (descending)	26 Mar 2015 – 29 Dec 2018 (*2,868*)	7,181,599	−11.0 – 10.9	0.3	24.0

- Minimum cluster size, which is referred to the statistically relevant minimum number of MPs to perform spatial clustering.

Taking into account the scale of analysis, it has been implemented an iterative procedure aimed at fine-tuning the displacement rate threshold based on the standard deviation (σ) of velocity, following already existing literature approaches (Barra et al., 2017; Solari et al., 2019; Tomás et al., 2019). A final stability threshold of ± 1 cm/year, corresponding to slightly more than 3σ, was here set to distinguish active MPs from stable ground reflectors. Keeping in mind the spatial resolution of the P-SBAS results (about 80 m × 80 m), every ground pixel is here inscribed within a 100 m radius buffer, a minimum number of 3 contiguous MPs was chosen to execute spatial clustering, implying that MACs with an extent lower than 3 times the dataset spatial resolution are not detected (about 0.02 km^2). Thirdly, the average displacement value and coherence of the MPs included in each cluster were automatically derived (as part of the model geoprocessing chain) in order to retrieve relevant statistical features for every deformation area.

The abovementioned parameters are not subjected to fixed rules; any sensitivity analysis regarding the impact of the specific parameter selection is neglected, considering that they should be tailored to the features of the given interferometric dataset and to the scope of the analysis.

It can be deduced that the expected output, generated in a shapefile format, consists of polygonal clusters which in turn might represent an approximation of the detected deformational processes in terms of planar extension. However, this kind of analysis constitutes nonetheless an accurate and quick method to systematically identify and locate sectors of the Italian territory where ongoing deformations due to geological processes are taking place.

2.2.2. *LOS velocity vectors decomposition*

P-SBAS provides deformation values measured along the radar line of sight, thus representing only a one-dimension estimation of the real motion. Reprojecting the velocity deformation vectors along the vertical (Up-Down direction) and horizontal (East-West) direction is a useful practice to enhance the deformation estimates and the classification of the observed phenomena (De Luca et al., 2017; Manzo et al., 2006; Notti et al., 2014), which can be done when ascending and descending datasets are available and when the contributions of N-S horizontal motions are assumed negligible (due to the intrinsic limitation of the satellite acquisition geometry). The computation of the vertical and horizontal components is performed by solving two simple equations, as pointed out by Notti et al. (2014):

$$V_V = \frac{((V_D/\mathrm{elos}_D) - (V_A/\mathrm{elos}_A))}{(\mathrm{hlos}_D/\mathrm{elos}_D - \mathrm{hlos}_A/\mathrm{elos}_A)}; V_H = \frac{((V_D/\mathrm{hlos}_D) - (V_A/\mathrm{hlos}_A))}{(\mathrm{elos}_D/\mathrm{hlos}_D - \mathrm{elos}_A/\mathrm{hlos}_A)}$$

where V_V and V_H are the vertical and the horizontal velocity components, V_A and V_D are the ascending and descending (LOS) velocity vectors; $\mathrm{hlos} = \cos(\alpha)$ and $\mathrm{elos} = \cos(1.571 - \alpha) * \cos(4.712 - \theta)$, where θ and α are the azimuth and the incidence angle respectively.

In order to retrieve V_V and V_H, we consider each pixel on the ground

for which we have both ascending and descending LOS velocity values (Fig. 4a). The vertical and horizontal components of the velocity can be thought as coordinates depicting the magnitude and the direction of the movement for each MP. Therefore, by representing the horizontal velocity on the x-axis and the vertical velocity on the y-axis it is possible to retrieve the "real" velocity vector, which can be plotted on the Up-Down and East-West plane. In order to help through an accurate visualization of the direction of the "actual" observed motion, it is here introduced a colormap (Fig. 4b) which is based on the ratio between the vertical and horizontal components of deformation. In this way, from (*i*) Up-East to (*ii*) East-Down, from (*iii*) Down-West to (*iv*) West-Up, 12 patterns of movement are highlighted.

For this research, the ratio between the vertical and horizontal motion components is retrieved and associated to every MAC for classification purposes (see section 2.2.3). On the other hand, detailed analyses at local scale is carried out by investigating the deformation pattern in depth and by fully exploiting the availability of spatially coincident LOS measures from both geometries.

2.2.3. *Rationale of motion areas classification procedure*

The desirable outcome of the proposed post-processing chain is the identification of the cause which leads to the ground deformations outlined by the spatial clustering results. The deforming area can be thought as an effect of natural processes or man-made activities (Matano, 2019). The model developed for the classification task consists of a chain of 8 different built-in GIS tools which focus on the quantification of the spatial relationship between features and on conditional statements dealing with threshold values. In order to make the model run, it is necessary to supply a mandatory polygon shapefile in input (*i.e.*, the MAC dataset), the ancillary maps when available and the slope map of the area of interest. Moreover, the model requires to specify the working folder and to set 4 parameters, namely a series of threshold values which can be summarized as follow: (*i*) percentage of spatial overlap; (*ii*) the mean vertical and horizontal components ratio values; (*iii*) the mean vertical component value; (*iiii*) the mean slope value. The decision tree and the specific parameter setting adopted in our case study is depicted in Fig. 5. Based on the working scale and the DInSAR data resolution, a spatial overlap between S1 data and ancillary dataset of at least 50% is here considered valid for a correct classification. According to the spatial correlation existing between the active motion areas dataset and the pre-existing inventories or ancillary maps, each MAC could be initially discriminated into 8 categories (Fig. 5): earthquake-induced deformations, volcanic-related processes, landslides, land subsidence, mining activities, dump site activities, construction site activities (where the latter three can be summarized as man-made activities) and unclassified. The last class is retained for the elements falling outside the classification criterion (*i.e.*, concomitant unavailability of the ancillary information and lack of interferometric data from the two geometries of acquisition). Any further distinctions or interpretation regarding the underlying natural or anthropic process (*i.e.*, settlements, sinkholes, natural or anthropogenic subsidence, etc.) which led to ground deformations are not considered because of the lack of comprehensive ancillary information and because out of the scope of this work.

For the deforming areas that lack of spatial correlation with the available ancillary data, the information retrieved from the 2D decomposition of LOS displacements is exploited. In order to interpret the underlying process which has led the ground to deform, it's here introduced the variable K_{VH} expressing the prevailing direction of the areal movement that has been derived for every MAC, that is the mean ratio between the absolute vertical (Up-Down) and the absolute horizontal (East-West) component values:

$$K_{VH} = \frac{|V_V|}{|V_H|}$$

where the different ratio values of spatially coincident MPs are averaged and related to every MAC.

The outcome of this computation, in combination with the computed average slope value, strengthens the association of MAC to 3 other possible categories (Fig. 5): potential landslide, potential subsidence, potential uplift. In particular, assuming that mass wasting processes are generally developed on slopes higher than 5° (Iwahashi et al., 2003; Lee et al., 2004; Tomás et al., 2019) and land subsidence likely occurs on plains or valleys floor (slopes less than 5°), moving areas showing a prevailing mean horizontal direction ($|V_V|/|V_H| < 1$) are here considered potential landslides, while moving area showing a prevailing mean negative vertical movement ($V_V < 0$ and $|V_V|/|V_H| > 1$) are considered potential subsidence. Upward vertical displacements can take place in different environments as a result of several factors (Bonì et al., 2018; Coda et al., 2019), thus MAC with a prevailing mean positive vertical movement ($V_V > 0$ and $|V_V|/|V_H| > 1$) are here associated to potential

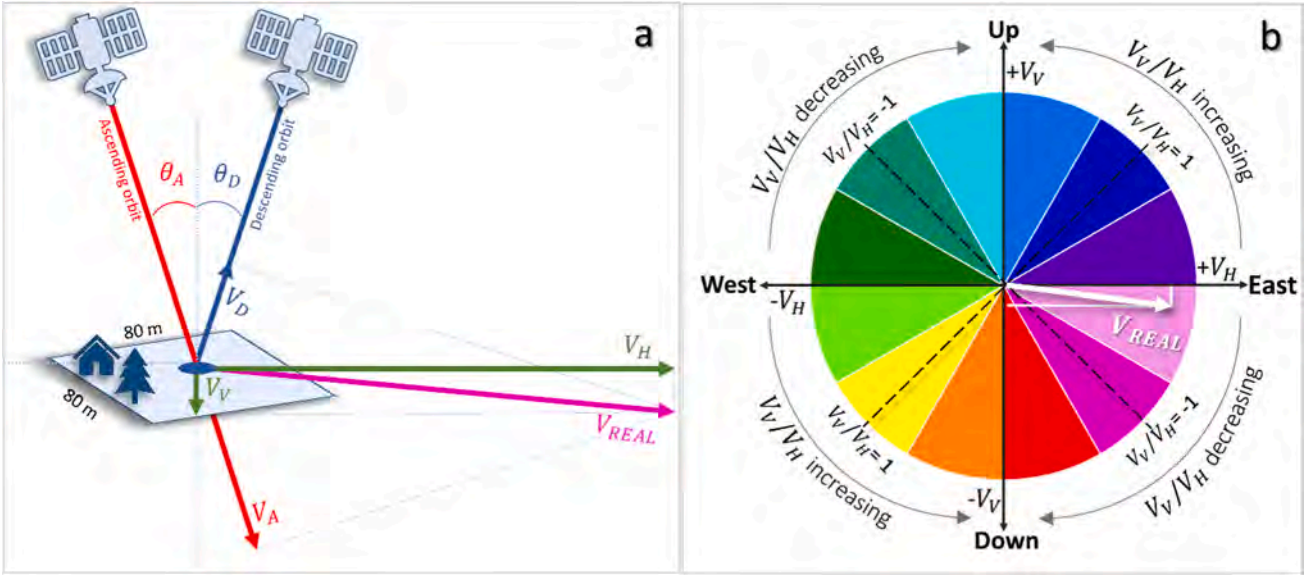

Fig. 4. (a) Resolving the E-W (horizontal) and the Up-Down (vertical) components of the LOS velocity within a MP; (b) polar plot of the "real" velocity vector projected on the Up-Down and East-West plane, where the different colours are associated to different directions, thus enabling a better comprehension of the pattern of movement.

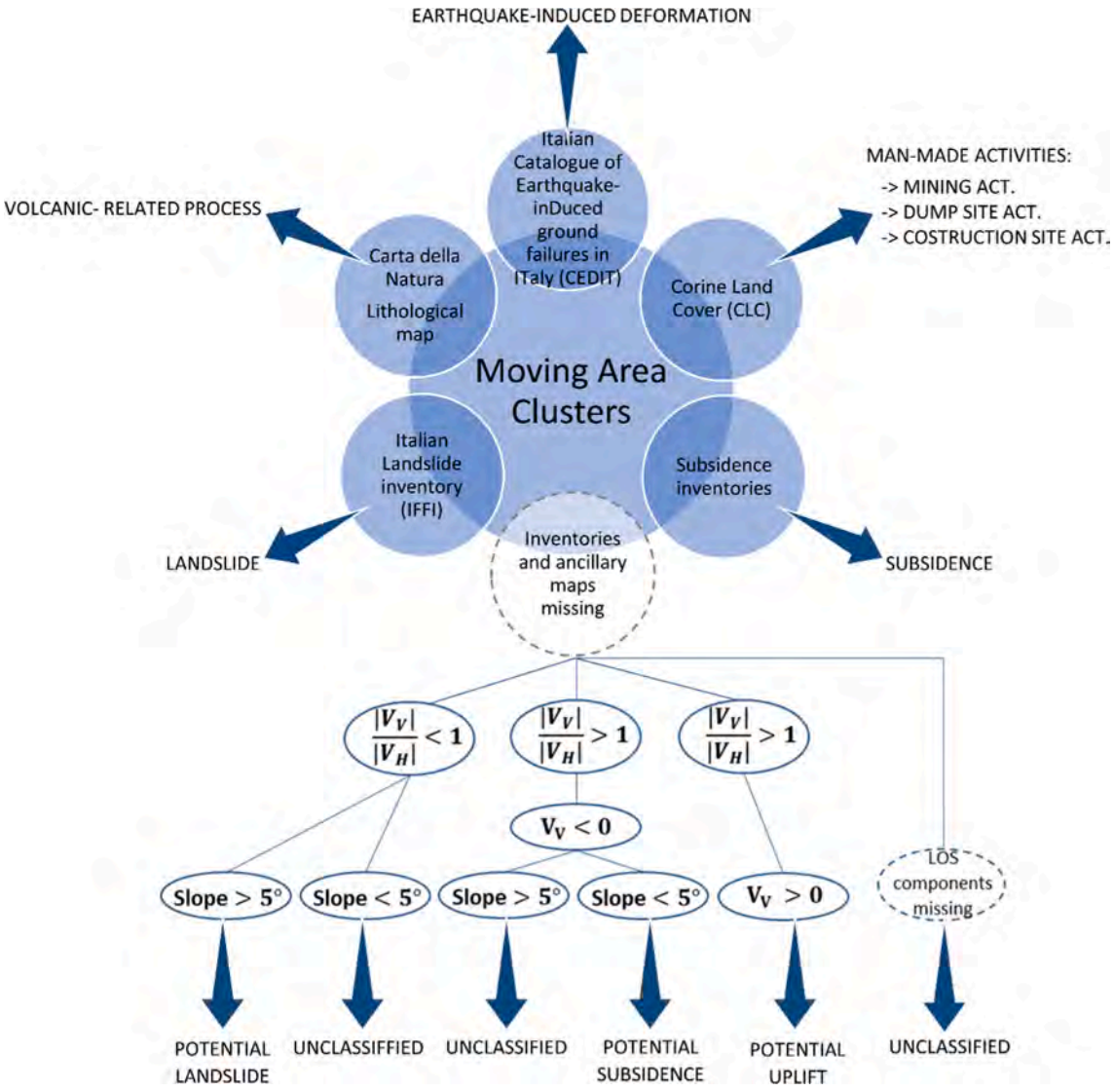

Fig. 5. Procedural scheme for the classification of Moving Areas Clusters (MAC).

uplifts. The adopted classification method operated through K_{VH}, slope and V_V thresholds (Fig. 5), arises from literature approaches (Tomás et al., 2019) and is supported by an a posteriori analysis carried out by extracting range values of the above-mentioned parameters from MAC overlapping with pre-existing geohazard inventories and ancillary maps. On the other hand, MAC whose K_{VH} and slope extracted mean values do not fall within the expected range, are labelled as unclassified.

3. Results

The results obtained by means of spatial clustering analysis and through the cross-correlation between the generated MAC and different collected maps covering the whole Italian territory are here described in three different sub-sections: (*i*) general characteristics of the computed country-wide active motion areas database; (*ii*) outcome of the performed classification; (*iii*) presentation of seven case studies, representative of the adopted classification, wherein the validation of the approach is also shown.

3.1. Characteristics of the moving area clusters database of Italy

Following the criteria explained in Section 2.2, a MAC database covering the whole Italian territory has been retrieved for both the ascending and descending input DInSAR datasets. The attributes related to the computed active motion areas are summarized in Table 2. The table fields include the average LOS velocities for both geometries, the number of MPs falling within every deformation area, the E-W and the vertical component of the LOS velocities, and the classification of the cause from which every MAC originated from.

The overall detected MACs are 14,638 which are differently distributed among the belonging DInSAR geometry: 8,278 clusters for the ascending geometry and 6,360 clusters for the descending one (Fig. 6a and Fig. 6b, respectively). The first set of MAC covers around 1,647 km^2 while the second covers around 1,223 km^2 which correspond respectively to ca. 3% and 2% of the ascending and descending deformation maps (where the areal extent of each MP is 80 m × 80 m). The difference between the two subsets is mainly due by the relatively smaller MP total count and MP density of the input descending DInSAR dataset. The mean LOS velocity distribution of the ascending and descending MAC has been computed and it is displayed in Fig. 6c and Fig. 6d: 85.2% and 87.4% of both datasets, respectively, show mean velocity values ≤ -1.0 cm/year, thus demonstrating a large predominance of deformation areas with a mean negative LOS velocity (movement away from the satellite sensor). Only 14.1% of the ascending and 12.2% of the descending areas indicate mean LOS velocities $\geq +1.0$ cm/year (movement towards the satellite sensor). Very few areas with

Table 2
The Moving Areas Clusters (MAC) database is provided with non-quantitative details and with statistical features related to the areal extent of the deforming area, the LOS, vertical and horizontal velocities and the temporal coherence (Pepe and Lanari, 2006).

Field	Description	Units
ID	Identification number of the active motion area	–
Satellite-orbit	Geometry of acquisition of the MPs from which the active motion area has been generated	–
Areal extent	Computed polygonal surface area	km^2
Mean coherence	Computed mean temporal coherence value of the MPs falling within the active motion area	–
Count MP asc	Number of ascending MPs falling within the active motion area	–
Count MP desc	Number of descending MPs falling within the active motion area	–
Mean VLOS asc	Computed mean ascending LOS velocity	cm/yr
Mean VLOS desc	Computed mean descending LOS velocity	cm/yr
Mean V_H velocity	Computed mean E-W component of velocity	cm/yr
Mean V_V velocity	Computed mean Up-Down component of velocity	cm/yr
Mean V_V/ V_H	Computed mean ratio between Up-Down and E-W component	–
Classification	Classification of the underlying ground deforming process	–

values between −1.0 cm/year and + 1.0 cm/year results from the spatial clustering operation considering that possibly MPs with opposite signs coexist in the same clustered area (due to an abrupt change of movement direction recorded within a very small distance).

The ascending and the descending MAC databases are here compared in terms of areal extent with the lithological map of Italy (1:500 000 scale) and the II level CLC (Corine Land Cover) map. By comparing the MAC coverage (MAC area within class/total class area) with respect to the total MP coverage (MPs area within class/total class area), it is possible to obtain a weighted measure (*i.e.*, the percentage of MAC area within class/MPs area within class) of the extent to which every lithological and land cover class has been affected by surface deformations during the monitored period (Fig. 7). Considering MAC belonging to both geometries, it is found that they are mainly located on effusive igneous rocks (7.7% for the ascending and 7.8% for the descending) and pelitic flysch (8.4% and 6.3%), followed by clay and marls (6.8% and 6.4%). Very few deforming areas are found to be spatially coincident with glacial deposits (from 0.1% to 0.2%) and with intrusive igneous rocks.

Concerning the distribution of MAC between land use classes, it is reported a clear disparity between the agricultural areas and the artificial surfaces, with the latter generally not much interested by deformational phenomena. Except for the mine, dump and construction sites (7.8% for the ascending MAC and 7.7% for the descending one), the majority of ground-moving zones is positioned on inland waters, open space with little or no vegetation and maritime wetlands. Compared to the coverage of the MPs, very few MAC are found on artificial, non-agricultural vegetated areas (0.3% for the ascending and 0.2% for the descending dataset) and on urban fabric (0.7% for both datasets). The significant presence of MAC within inland waters is due to the proximity of deformation areas to water bodies, where the clustered MPs mainly refer to dynamic environments such as river banks, shores and cliffs.

3.2. Classification of the active motion areas

The active motion areas have been classified according to the spatial association existing with the geohazard-related inventories and ancillary maps as outlined in Fig. 5. In terms of covered area, the overall partitioning of the ascending and descending active motion areas between the various categories is comparable (Fig. 8) with some discrepancies induced by the different satellite view. The descending dataset has recorded a relative majority of volcanic-related processes (24.8%) with respect to the ascending dataset (19.5%). An opposite trend arises for the earthquake-induced deformations, which constitute 11.9% of the descending clusters and 17.1% of the ascending ones. Other minor mismatches regard the percentage of subsidence-related events (6.7% of the ascending areas and 7.5% of the descending areas), the fraction of deforming areas positioned on previously mapped landslides (12.0% and 13.8% respectively) and the percentage of not classified phenomena (4.8% of the total area covered by the ascending dataset vs. 2.7% of the descending one). The remnant categories show differences in the range of ca. one percentage point.

If active motion areas categorized as landslide and potential landslide are considered together, it appears that slope instabilities processes could be considered as the most representative phenomenon in the ascending and descending datasets (30.8% and 31.4% respectively). On the contrary, both the potential uplifts and the man-made activities (*i.e.*, dump site activities, construction sites activities and mining activities) constitutes together the minority of the two datasets (Fig. 8).

Moreover, an average value of slope and elevation has been computed on the deforming areas belonging to the various categories (Table 3). Nearly identical values (around 19° of slope and elevation comprised between 813 and 833 m.a.s.l.) are shared between the two datasets for the earthquake-induced deformations, due to the geographical coincidence of the underlying motion areas which correspond to the seismic sequence occurred on 2016–2017 in the Central Apennines. The active volcanic-related processes are likewise reported in the same locations in both ascending and descending MAC (Fig. 8): they describe the Mount Etna (an active stratovolcano on the East coast of Sicily) and the Phlegraean Fields (a vast area of volcanic origin located North-West of the city of Naples which has been historically affected by bradyseism) ongoing deformations. In this case the exact geographical position of the MAC is changing, as well as the average slope and the average elevation, according to each orbit.

The distribution of the MAC classified as landslide and subsidence totally reflect the physiographic pattern of the Italian peninsula, with the first category to be found throughout the Apennine chain and the Alpine chain while the second to be placed on the main Italian plains, such as the Po Plain (northern Italy) or the Tavoliere delle Puglie (south-eastern Italy). Accordingly, an average slope value of 14.3° – 15.0° (respectively in the ascending and descending dataset) for the deforming areas marked as landslides while an average slope of 0.4° is attributable to the subsidence-related clusters. A similar trend is confirmed when looking at the average slope and elevation values of MAC classified as potential landslide and potential subsidence (Table 3). However, the difference appears to be less pronounced, with a mean slope of 1.6° – 1.5° for potential subsidence phenomena and a mean slope of 12.5° – 13.0° for potential landslides (respectively in the ascending and descending dataset).

Among the remaining categories (*i.e.*, potential uplift and the man-made activities), the mining activities account for the highest percentage of covered area together with the highest average slope and elevation value.

3.3. Case studies

In this section, 7 specific cases, classified according to the different triggering mechanism, are illustrated, showing the large applicability in different scenarios of the MAC algorithm on interferometric results.

3.3.1. Landslide - Maratea municipality (Basilicata Region)

Fig. 9 illustrates the case study of a moving area located at Maratea, in the Potenza province (Basilicata Region, Italy). The Maratea Valley is known for being historically affected by large complex deformational phenomenon which are thought to be firstly controlled by the geological setting and, secondly, by the active role played by tectonics in that area

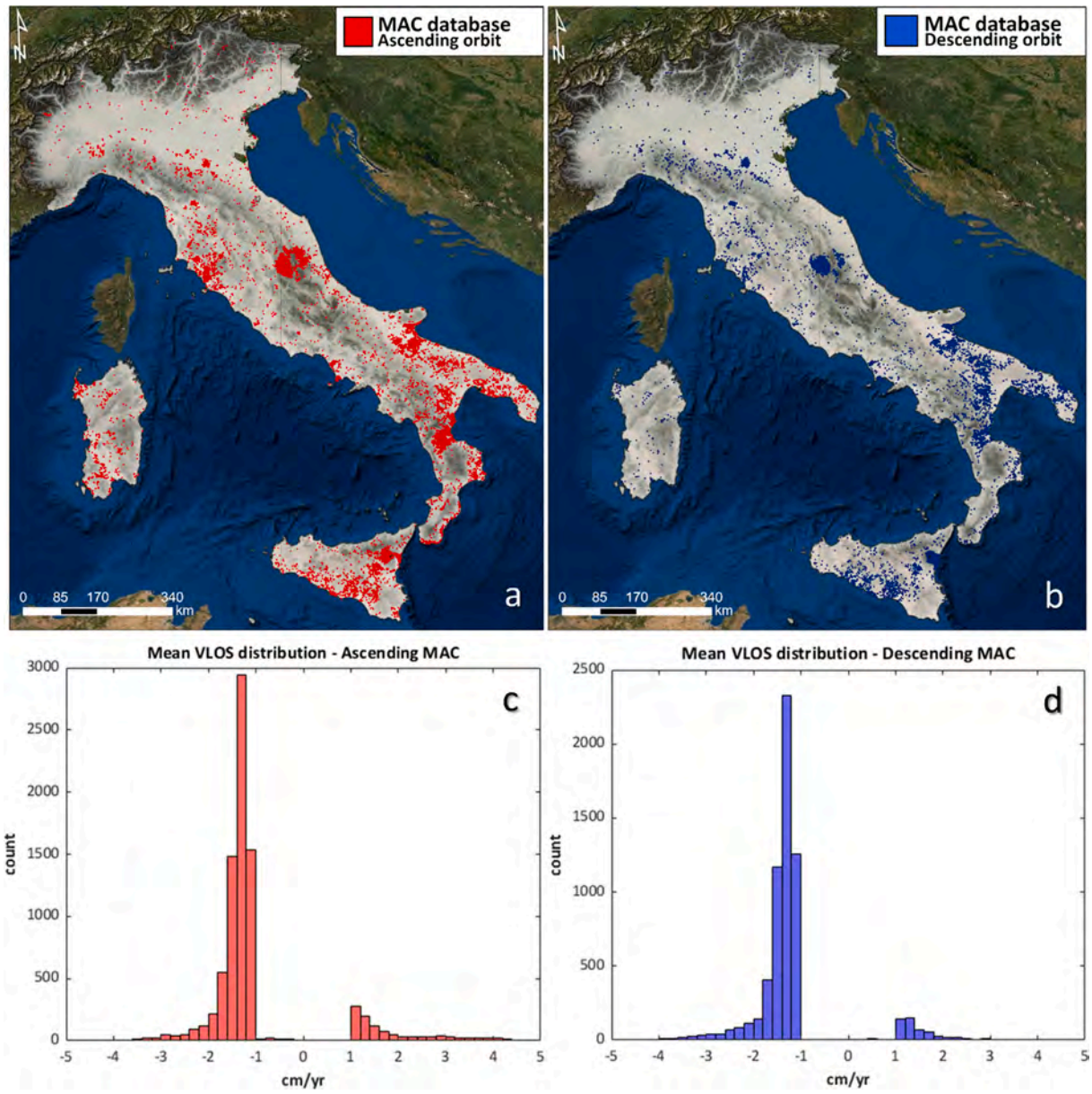

Fig. 6. (a) The ascending and (b) the descending Moving Areas Clusters (MAC) database for the reference period March 2015- December 2018 resulting from the spatial clustering analysis performed over the whole Italian territory and (c, d) the mean VLOS value distribution computed for the ascending and the descending MAC, respectively.

(Berardino et al., 2003; Rizzo, 2002). As a result of several studies, it is reported that the village of Maratea rises on a composite DSGSD (deep-seated gravitational slope deformation) which can be described as a spreading evolving lower-down into a large and deep flow, due to the superimposition of permeable and rigid masses (carbonate units, breccia and detritus) upon plastic ones (clayey flysch). The movements monitored on the surface and in depth, referred to the period 1992–1996 and reported by Rizzo and Limongi (1997), are both of the order of 2–4 cm/year.

The slope deformation affecting the study area has remained active for the reference period March 2015-December 2018 as it is recorded by both the ascending and descending MAC database; an overall mean LOS velocity of 1.5 cm/year and −1.6 cm/year respectively for both geometry of acquisition is reported, where the positive value indicates movement towards the satellite while the negative sign implies movement away from the satellite. Within the boundaries of the detected moving areas, a peak velocity of −2.6 cm/year on the eastern sector is reached (Fig. 9a; Fig. 9b). The areal extent of the detected deformation ranges between 2.4 km^2 (descending MAC) and 2.6 km^2 (ascending MAC) and it covers almost all of the residential settlements located on the northern side of the Mt. San Biagio.

Focusing on the deformation pattern, the entire ground displacement follows a general westward horizontal direction ($|V_V|/|V_H| < 1$), however, while the steepest and easternmost sector of the MAC (represented with light-green MPs) has moved slightly downward, the flat sector located on the valley floor has undergone a relative upward deformation (Fig. 9c). By observing the ground deformation as seen by satellites from two points of view (ascending and descending geometry of acquisition), the kinematic behavior of the DSGSD can be inferred: a progressive downslope shift from negative to positive vertical displacements can be linked to a semicircular or compound failure plane (Frattini et al., 2018). The real velocity vectors (Fig. 9d) have recorded a maximum rate of deformation of 3.8 cm/year, thus falling inside the range of the GPS measures observed by Rizzo (2002) in the inhabited area of the valley.

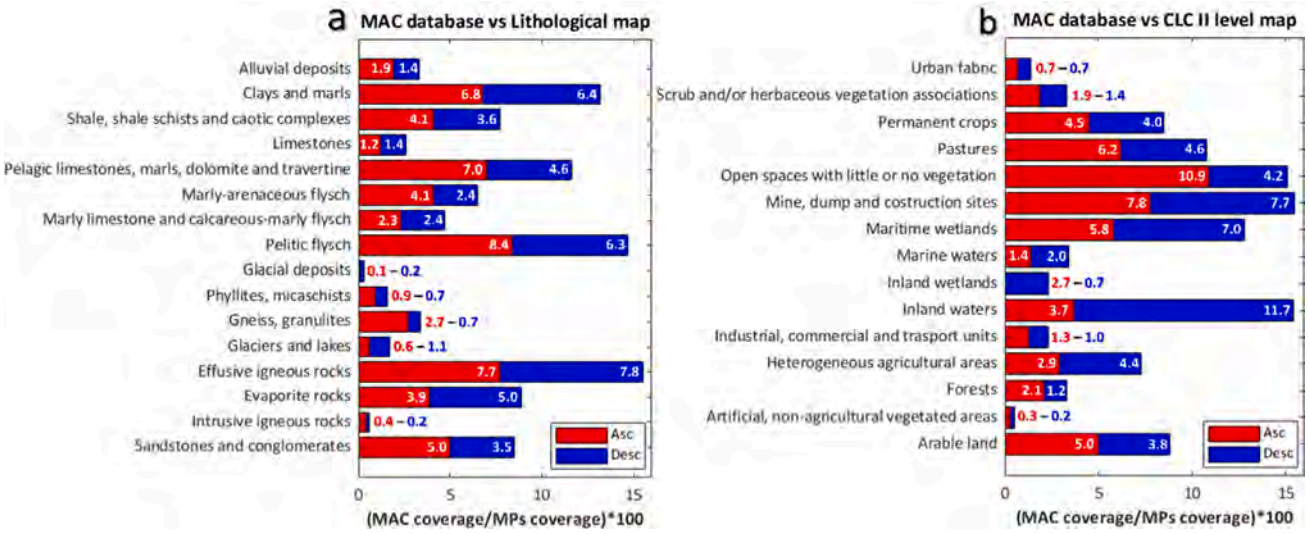

Fig. 7. Comparing the coverage of the ascending and the descending Moving Areas Clusters (MACs) with respect to the coverage of the Measurement Points (MPs, constituting the ascending and descending velocity deformation maps) for each categorical class of (a) the 1:500 000 lithological map of Italy and of (b) the second level of the Corine Land Cover map.

3.3.2. Volcanic-related process - Phlegraean Fields (Campania Region)

In Fig. 10, the case of one of the most studied volcanic areas in the world, the Phlegraean Fields caldera, is presented. This area is located along the western coast of the Campania Region (southern Italy) in a largely urbanized territory, including the western sector of the city of Naples. The present physical aspect of the Phlegraean Fields can be considered as the result of two recent major eruptions, *i.e.*, the Campanian Ignimbrite (~39 ka) and the Neapolitan Yellow Tuff (~15 ka), which produced two nested calderas covering together a 16 km wide area (Acocella, 2008; Bevilacqua et al., 2020; Fedele et al., 2011). At least since 2nd Century BCE the Phlegrean Fields have undergone a bradyseism phenomenon consisting of several uplift and subsidence episodes. Since 2005, after a 20 years-long phase of subsidence, the caldera has been experiencing a phase of uplift movement, registering a slow acceleration in the last years (Bevilacqua et al., 2020; Chiodini et al., 2017; D'Auria et al., 2015; Patra et al., 2019) and a total maximum vertical displacement in the *Pozzuoli* area of ca. 83 cm (recorded up to June 2021) (Osservatorio Vesuviano, 2021).

The recent uplift movement is confirmed by the DInSAR dataset and the consequent MAC database, where both ascending and descending deformation clusters fall East and West of the Pozzuoli Bay covering an area of 33.5 km^2 and of 33.2 km^2, respectively for a total area of 58.2 km^2 (without considering the overlapping parts of the two clusters). For the reference period March 2015-December 2018, the recorded peak velocities of 6.2 cm/year (ascending geometry) and of 6.5 cm/year (descending geometry) are referred to MPs falling exactly inside the Pozzuoli district (Fig. 10a; Fig. 10b).

Considering the LOS velocity projected on the Up-Down and East-West plane, it emerges that the spot with the highest deformation rate (*i.e.*, the *Pozzuoli* district) shows MPs holding vertical component of displacement considerably greater than the horizontal ($|V_V|/|V_H| > 1$); that zone seems to acts as a ridge zone dividing the western sector and the eastern sector into areas uplifting with a westward and eastward component respectively (Fig. 10c). The polar plot represented in Fig. 10d displays that the maximum displacements have acted vertically close to the center of Phlegraean Fields caldera (located in the town of *Pozzuoli*) with the magnitude of the "real" velocity reaching a peak velocity of 8.6 cm/year during the monitored period (Osservatorio Vesuviano, 2018). On the other hand, on the outermost parts of the clustered areas, the entity of the displacements decreases in intensity with the horizontal component of motion increasing in parallel. The highlighted results confirm that the ground deformations are located over a semi-circular annular Region and follow a radial pattern both in terms of intensity and orientation (Bevilacqua et al., 2020; Manconi et al., 2010).

3.3.3. Earthquake-induced deformations - the 2016 Amatrice-Visso-Norcia seismic sequence (central Italy)

In Fig. 11 the mapped coseismic surface deformations related to the Amatrice-Visso-Norcia seismic sequence that struck central Apennines between August and October 2016, as a result of the S1 P-SBAS processing are shown. The sequence initiated on 24 August 2016 with the Moment magnitude (M_w) 6.0 Amatrice earthquake claiming at least 290 lives and causing widespread damages. On 26 October 2016, another M_w 5.9 earthquake hit the village of Visso, which is ca. 25 km to the North of Amatrice. The largest seismic event, the M_w 6.5 Norcia earthquake, occurred on 30 October and nucleated in an area comprised between the two previous events. The following months an intense aftershock activity involved the activated zone, which runs NNW-SSE parallel to the axis of the central-northern Apennines (Improta et al., 2019).

The detected moving areas (which occupy a total area of ca. 70 km × 70 km) correspond to coseismic short-term displacements and long-term post-seismic ground deformations related to the Amatrice-Visso-Norcia seismic sequence. Surface deformations due to different phenomena (e.g., slope failures, anthropic activities…) that possibly affected the same area during the monitored period March 2015 - December 2018 could not be inferred solely on the basis of the mean deformation velocity.

The ascending and descending MAC database predominantly recorded displacements in the areas surrounding the activated zone, which is roughly located along the three mainshock epicentres (Fig. 11a and Fig. 11b, respectively). The absence of interferometric data in the vicinity of the hypocentral area has to be ascribed to the loss of coherence because of temporal changes in the scattering conditions on the ground (Kobayashi et al., 2012). The observed displacements are characterized by two NNW-SSE striking deformation lobes with positive and negative velocities depending on their position respect to the epicentres and to the geometry of acquisition of satellites (Fig. 11a; Fig. 11b) with values reaching a peak of 5.8 cm/year on the left of the activated zone, where it is also recorded a higher density of MAC. This trend clearly confirms the widely accepted hypothesis of a normal fault mechanism for the Mw 5.9–6.5 mainshock events, where the coseismic collapse of the hanging wall accounted for the main visible displacement.

Through the analysis of the displacement on the Up-Down and East-

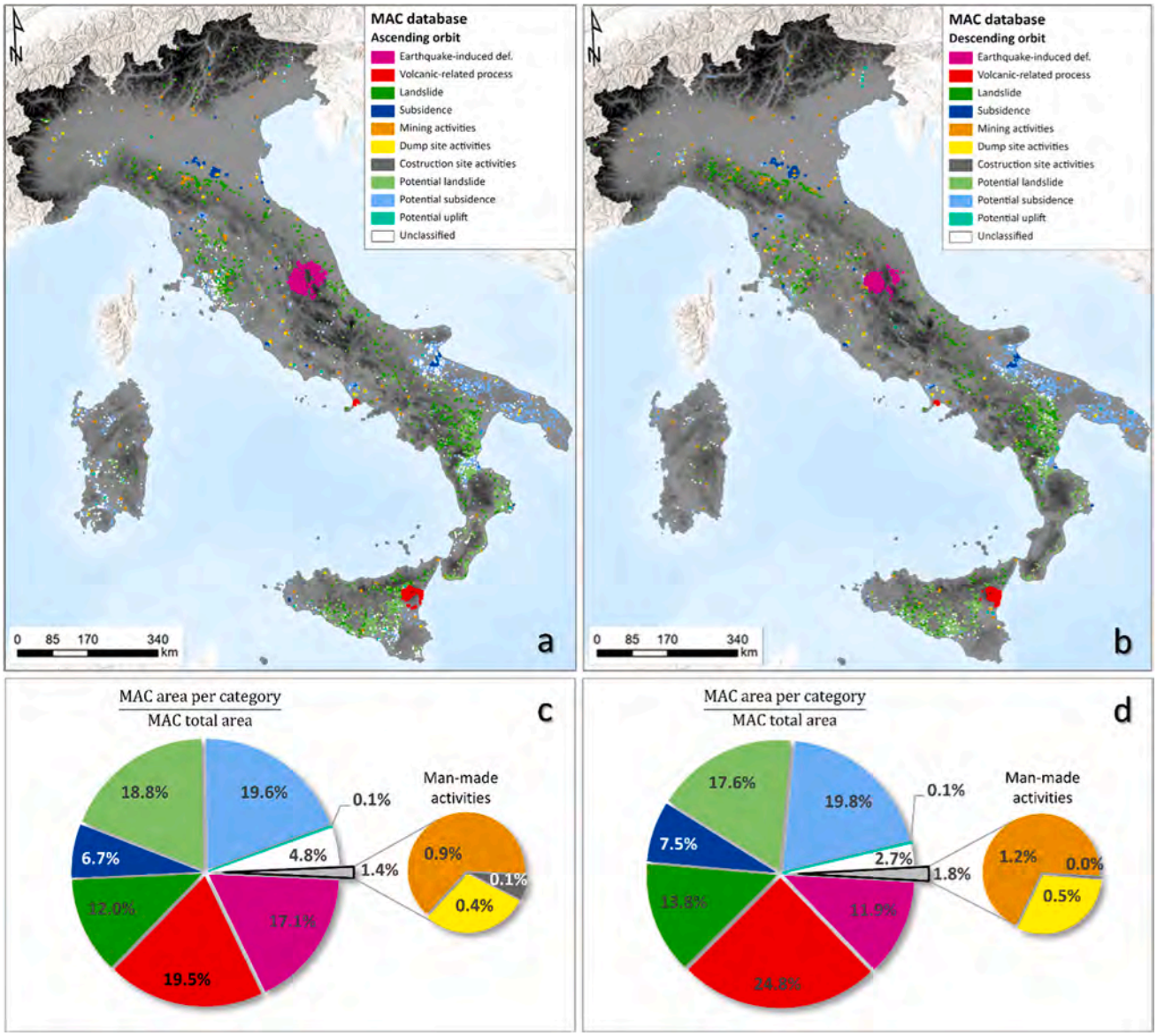

Fig. 8. Classification of the (a) ascending and (b) descending moving area clusters (MAC) of Italy retrieved for the reference period March 2015-December 2018. Pie charts showing the (c) ascending and (d) descending MAC distribution within the different categories, in terms of covered area respect to the total area of each MAC database.

West plane, the area hit by the 2016 seismic sequence reveals a complex pattern of deformation (Fig. 11c). Despite the large number of MPs throughout the site of interest holding very different values of ratio between the vertical and the horizontal velocity components, it is here highlighted the E-W component of deformation concerning the two deformation lobes, with the eastern one (corresponding to the foot wall area) shifted eastward and the western one (corresponding to the hanging wall area) shifted westward in agreement with previous studies (Cheloni 2017; Huang et al., 2017). Moreover, a clear subsidence pattern is partially visible in correspondence to the Amatrice village (marked with red and orange colours in Fig. 11c). The polar plot represented in Fig. 11d displays the "real" vectors with computed velocities considerably higher than the LOS ones: a maximum horizontal displacement of 8.4 cm/year has affected the central part of the left lobe (~7 km NW from Norcia village).

3.3.4. *Subsidence - Montemurlo municipality (Tuscany Region)*

The municipality of *Montemurlo*, in the Prato province (Tuscany Region), along with the Firenze-Prato-Pistoia basin, is an area historically known for being affected by subsidence phenomena. In particular, the southwestern portion of the municipality hosts a large industrial area, whose presence could be connected to the recent seasonal variation of the water table due to groundwater withdrawal (Del Soldato et al., 2019).

The MAC database shows two cluster of MPs in the ascending geometry with a total areal extent of 0.4 km^2 while the two equivalent detected descending deforming area are slightly larger (0.5 km^2). For the reference period March 2015-December 2018 the area has registered a peak velocity of −3.9 cm/year and of −4.2 cm/year in the cluster centres of the ascending and descending geometry, respectively (Fig. 12a; Fig. 12b).

In Fig. 12c, the computed components of displacement are visible, highlighting an expected pattern of deformation: the entire area suffered land subsidence resulting in a high value of mean absolute ratio between the vertical and horizontal components ($|V_V|/|V_H| > 1$), with the western sectors moving relatively towards East and the eastern sectors to the opposite direction (*i.e.*, towards West). This trend implies that the sinking of the central zone of the deforming areas (where land

Table 3
Statistics depicting the number and the area covered (both in absolute figures and as a percentage of the total), the average slope and the average elevation computed per every category into which MAC are classified.

Categories	Ascending orbit				Descending orbit			
	Count (%)	Area (%) km^2	Avg. Slope *deg* (°)	Avg. Elev. *m.a.s.l*	Count (%)	Area (%) km^2	Avg. Slope *deg* (°)	Avg. Elev. *m.a.s.l*
Earthquake-induced def.	1004 (12.1%)	282.3 (17.1%)	19.3	813.1	629 (9.9%)	145.8 (11.9%)	18.9	833.4
Volcanic-related process	150 (1.8%)	320.0 (19.5%)	8.1	779.7	148 (2.3%)	302.5 (24.8%)	10.6	876.5
Landslide	1349 (16.3%)	197.5 (12.0%)	14.3	417.9	1184 (18.6%)	169.2 (13.8%)	15.0	420.8
Subsidence	279 (3.4%)	109.7 (6.7%)	0.4	34.9	307 (4.8%)	91.9 (7.5%)	0.4	32.5
Mining act.	116 (1.4%)	14.9 (0.9%)	10.7	231.3	115 (1.8%)	14.9 (1.2%)	11.2	273.0
Dump site act.	40 (0.5%)	6.8 (0.4%)	4.2	117.9	36 (0.6%)	6.7 (0.5%)	4.5	133.6
Construction site act.	5 (0.1%)	1.6 (0.1%)	2.9	183.0	1 (0%)	0.1 (0.0%)	6.1	178.7
Potential landslide	2349 (28.4%)	310.0 (18.8%)	12.5	327.6	1765 (27.8%)	215.1 (17.6%)	13.0	335.4
Potential subsidence	2227 (26.9%)	323.5 (19.6%)	1.6	143.0	1856 (29.2%)	242.0 (19.8%)	1.5	146.0
Potential uplift	22 (0.3%)	1.7 (0.1%)	1.4	144.4	15 (0.2%)	1.3 (0.1%)	1.0	133.1
Unclassified	737 (8.9%)	79.0 (4.8%)	3.1	172.9	307 (4.8%)	33.6 (2.7%)	4.1	210.5

subsidence effects are more evident) may drive the surrounding movements. Hence, the interferometric results suggest the existence of a cone-shape depression radiating away from the centre of the clustered areas due to groundwater overexploitation. The polar plot represented in Fig. 12d shows a maximum "real" velocity (*i.e.*, computed on the Up-Down and East-West plane) of ca. 4.8 cm/year. Del Soldato et al. (2019) report average interferometric measures of ground velocities reaching approximately − 10 cm/year in July 2017 and June 2018 which nevertheless relate to rates of ground subsidence of particular intensity occurred in specific time spans.

3.3.5. *Dump site activites - Masseria del Re storage site (Campania Region)*

Masseria del Re, a locality that belongs to the municipality of Giugliano in Campania, gave its name to the storage site located in the province of Naples (southern Italy). As a result of the recent crisis related to the disposal of waste in the Campania Region, the site has been designated since January 2006 as a storage space for tons of fuel pellets produced from waste of different origins. The accumulation of material continued until August 2007 up to the complete saturation of the site, where more than 5 million of fuel pellets have been amassed on a surface area of about 460,000 m^2. The regional authorities announced the start of work concerning the removal of waste from the site in May 2016.

The S1 derived MAC database referred to the monitored period March 2015-December 2018 shows ground deformation both in ascending and descending geometry covering the whole storage site (Fig. 13a; Fig. 13b). All the clustered MPs inside the two moving areas are characterized by negative LOS values, thus testifying the overall lowering of the zone where the fuel pellets are set. The estimated areal mean velocity ranges between −2.1 cm/year (as seen from the ascending orbit) and −2.5 cm/year (as seen from the descending orbit), while locally it is reached a maximum velocity of −5.4 cm/year.

While looking at the deformation pattern on the Up-Down and East-West plane (Fig. 13c), it emerges the clear predominancy of surface deformations acting vertically throughout the storage site ($|V_V|/|V_H| > 1$). The polar plot represented in Fig. 13d shows a maximum "real" velocity of ca. 6.9 cm/year, thus highlighting once again the importance of combining data from different geometries of acquisition for a better estimation of the entity of the displacement. Two main causes can be reasonably connected to the observed lowering deformation over the area of interest: (*i*) the fuel pellets load imposition with the subsequent ground lowering and (*ii*) the leachate production, collection and extraction which are regularly performed on site by the facility operators. As a result, it can be concluded that the observed motion is mainly related to the waste material load, rather than the local ground surface.

3.3.6. *Mining activities - Santa Barbara (Tuscany Region)*

The former Santa Barbara brown coal mining area is settled in the municipality of Cavriglia, in the Arezzo province (Tuscany Region). The mining activities started in 1860 and ended in 1994 due to exhaustion of the lignite basin. The topography of the site has drastically evolved with the site exploitation, with the formation of hills and ground excavations, where the latter have become today visible lakes (Bozzuto and Geroldi 2021). In particular, the slope close to the Allori Lake, due to his orientation eastwards and its artificial bare terrain, turns out to be greatly monitored from S1 satellite systems. The former mining site is currently object of an Environmental Rehabilitation Plan (Bozzuto and Geroldi 2021).

Two ascending clusters (Fig. 14a) are located on the above-mentioned slope, where the largest (0.5 km^2) is just in front of the Allori lake and the Bomba area (which is the seat of many warehouses) while the smallest (~0.1 km^2) is ca. 700 m north of the first cluster; one descending MAC (Fig. 14b), with an area extent of 0.6 km^2, occupies roughly the same position of the largest ascending cluster. A peak of LOS velocity of about −9.8 cm/year was recorded in the ascending geometry, during the monitored period March 2015 - December 2018, as well as an average displacement rate of −4.1 cm/year and −2.7 cm/year in the two ascending deforming areas. For what concerns the descending geometry, an average LOS velocity of 2.1 cm/year has been measured for the same area. On the contrary, the Bomba area appears to have slightly moved toward the satellite sensor (uplift movement) without generating any MAC, due to an estimated average ascending LOS velocity of 0.6 cm/year and an average descending LOS velocity of 0.3 cm/year in that zone (Fig. 14a; Fig. 14b). All the reported observations are consistent with the latest interferometric measurements available on the area of interest (https://geoportale.lamma.rete.toscana.it/difesa_suolo/#/).

In Fig. 14c the combination of ascending and descending LOS velocities has allowed a 2D reconstruction of the velocity vectors in the Up-Down and East-West plane: the overlapping clustered areas show an evident East-Down direction of movement, thus behaving similarly to a landslide process. This evidence is supported by the presence of several slope instabilities spread throughout the site of interest (Fig. 14). The polar plot represented in Fig. 14d shows a maximum "real" velocity of 9.2 cm/year within the perimeter of the outlined clusters, which is comparable to the peak LOS velocity recorded in the ascending DInSAR dataset. The "real" velocity vectors related to the Bomba area exhibit upward movement which has reached 1.5 cm/year at most during the reference period. In the context of abandoned coal mine sites which have undergone flooding, the uplift movement could be ascribed to the long-term complex interaction between the mine goaf, the rock mass and the

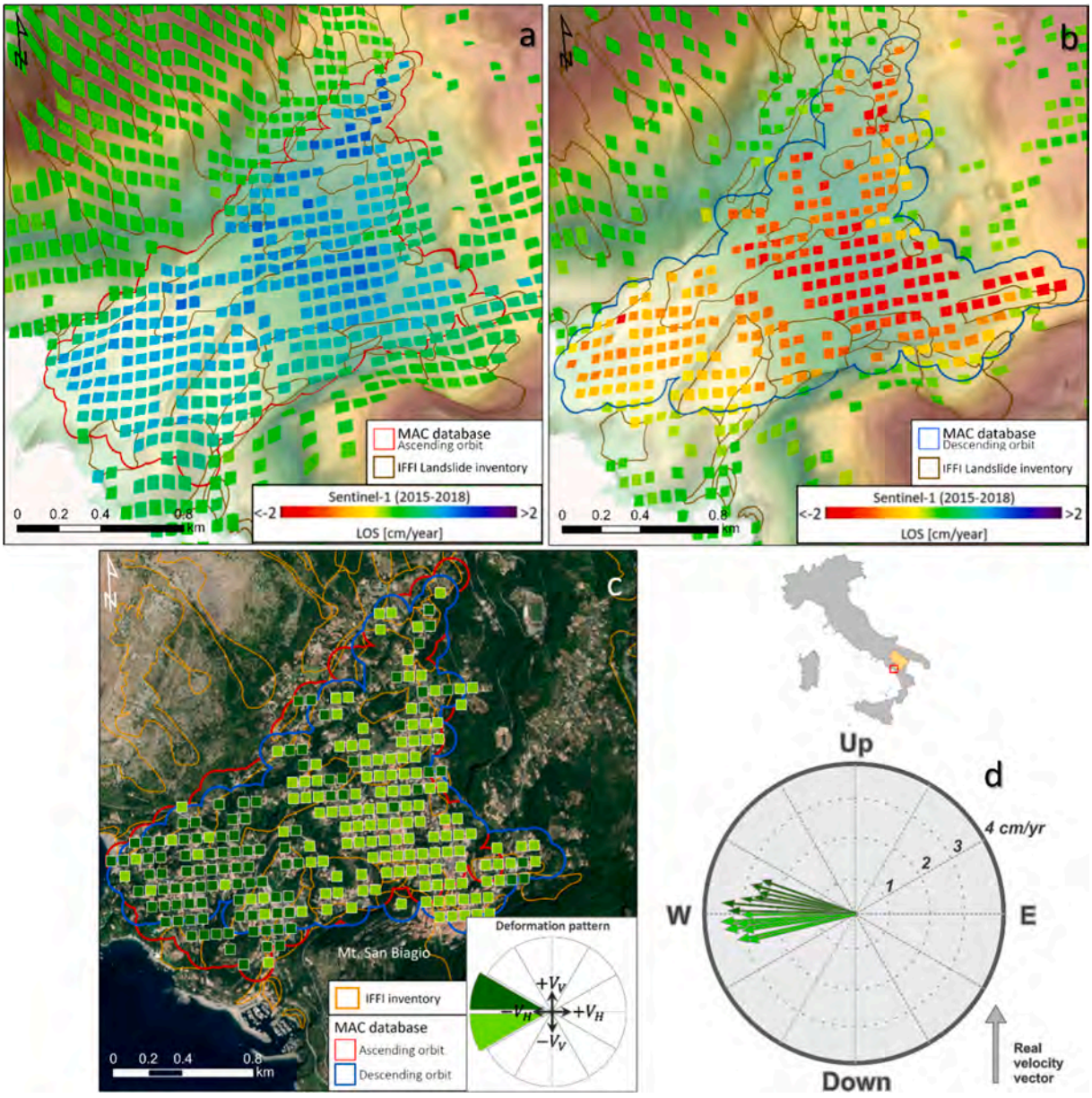

Fig. 9. Maratea municipality (Basilicata Region) results. a,b) 3D view of the ascending (a) and descending (b) deformation velocity maps; (c) vertical and horizontal component of the deformation velocity obtained by combining LOS ascending and descending MACs; (d) polar plot depicting a representative sample of the "real" velocity vectors computed for each MP within the two MAC of Maratea showing the magnitude and the direction of the movement on the Up-Down and East-West plane.

fluctuation of the groundwater level (Zhao and Konietzky 2020). The development of different lakes in the former mining area over the past century (*e.g.*, the Allori Lake) could have played a significant role in triggering the observed surface deformations.

3.3.7. Construction site activities - freight village Amerigo Vespucci (Tuscany Region)

The freight village Amerigo Vespucci is located in the municipality of Collesalvetti and represents the main container station for the Livorno province (Tuscany Region), due to its strategic vicinity to the developed infrastructural area where it sits. Today, the freight terminal covers a surface area of ca. 3,000,000 m^2, while the creation of the hub dates back to late'80 when the area was designed as a building site to be used for commercial and logistical-industrial use. Since the construction of the first warehouses, the area has been experiencing ground lowering due to the consolidation processes as a consequence of the buildings load imposition (Ciampalini et al., 2019), which resulted in structural damages to the sheds and consequent economic losses.

Two overlapping ascending and descending MAC with comparable extension concern the area corresponding to the freight village Amerigo Vespucci during the monitored period March 2015-December 2018 (Fig. 15a; Fig. 15b). It is reported an area mean velocity of −1.8 cm/year for both geometries, while locally observed ground displacements have reached a maximum of −3.7 cm/year. The freight station site appears to have been generally subducted, however few MPs within the clustered areas show to be within the range of stability (velocity ranging between −0.3 – 0.3 cm/year), thus highlighting that the area has possibly undergone a process of differential settlement, as also testified by Ciampalini et al. (2019).

In Fig. 15c the components of the LOS velocities on the Up-Down and East-West plane are shown, as a result of the combination of the ascending and descending interferometric data. The ground has

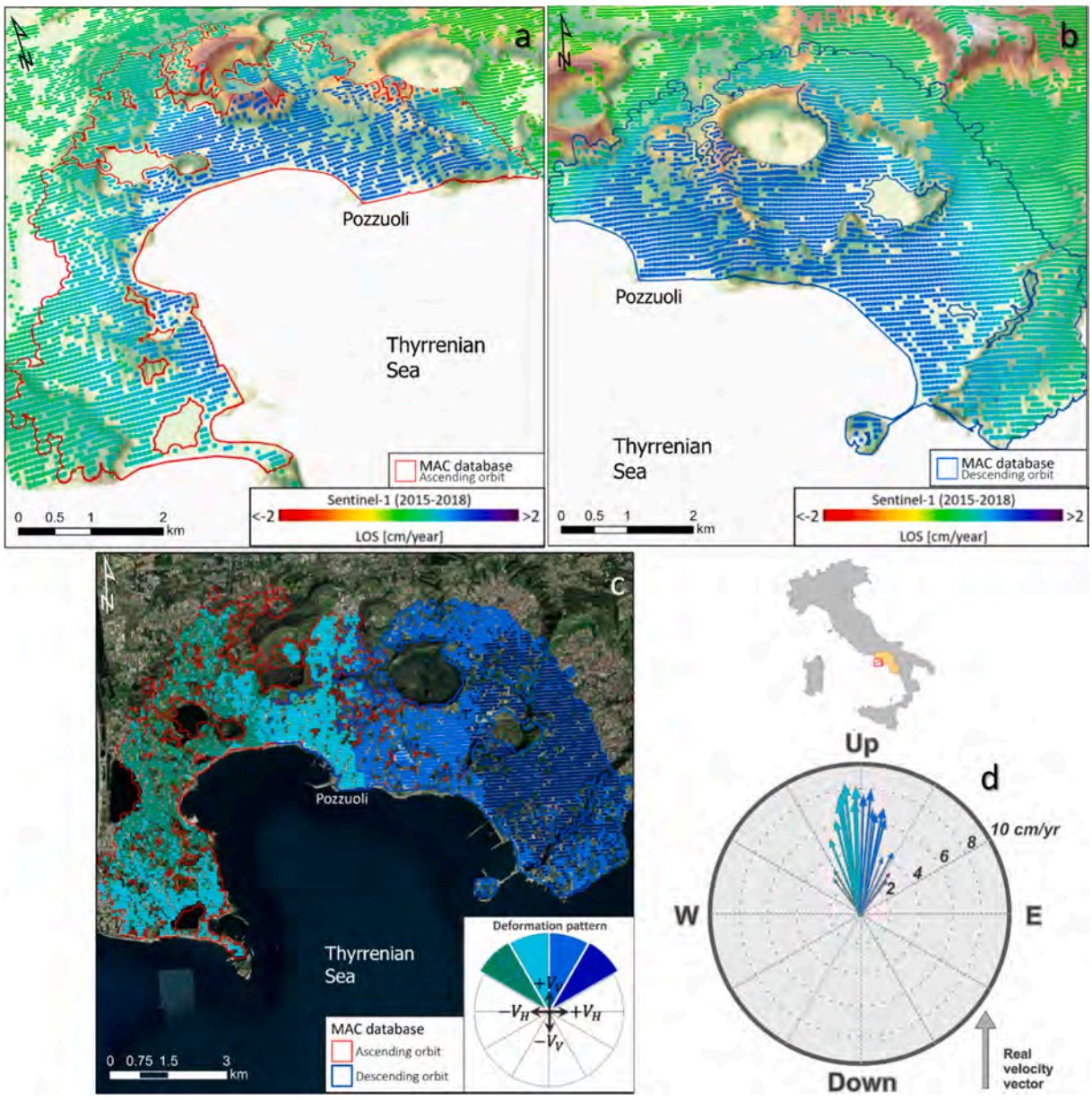

Fig. 10. Phlegrean Fields (Campania Region) results. (a, b) 3D view of the ascending (a) and descending (b) deformation velocity maps; c) vertical and horizontal component of the deformation velocity obtained by combining LOS ascending and descending MACs; (d) polar plot depicting a representative sample of the "real" velocity vectors for each MP within the two MACs, showing the magnitude and the direction of the motion on the Up-Down and East-West plane.

displaced in downward direction ($V_V < 0$ and $|V_V|/|V_H| > 1$) with a mean "real" velocity equal to 2.1 cm/year considering the entire area, while it is recorded a local peak of 7.2 cm/year (Fig. 15d) in the north-eastern sector of the freight village. The observed deformation pattern confirms the ongoing process of settlement caused by the consolidation of a highly compressible clay layer in response to building loads, while the observed measures are in good agreement with the rate of velocity derived for the same period from past studies conducted over this area (Ciampalini et al., 2019).

4. Discussion

In the framework of rapid detection and characterization of the most active ground motion phenomena affecting very large portions of a territory, the activity of filtering and mapping nation-wide DInSAR datasets proves to be a particularly useful technique in order to retain meaningful information related to ground deformation processes which normally concern the Earth surface.

The improvements that have been made in the field of the analysis and exploitation of the interferometric data move in parallel with the rising quality and quantity of SAR images, along with the continuous development of more precise and efficient DInSAR algorithms. The P-SBAS approach can meet the present need of boosting the efficiency in computing precise deformation maps out of extremely large Sentinel-1 SAR archives with a worldwide coverage and unprecedent temporal sampling. The present research demonstrates that, starting from continuous SAR-derived information, it is nowadays possible to obtain a periodical long-term mapping plan of the sectors of territories affected by relevant surface deformations, thus guaranteeing a support in the assessment of the location, the extent, the probable underlying cause, the magnitude and direction of movement of the detected phenomena.

The performance of the GIS-models adopted for this research demonstrates the applicability of our procedure to very large interferometric datasets, even with not high-performance machine. The equipment used

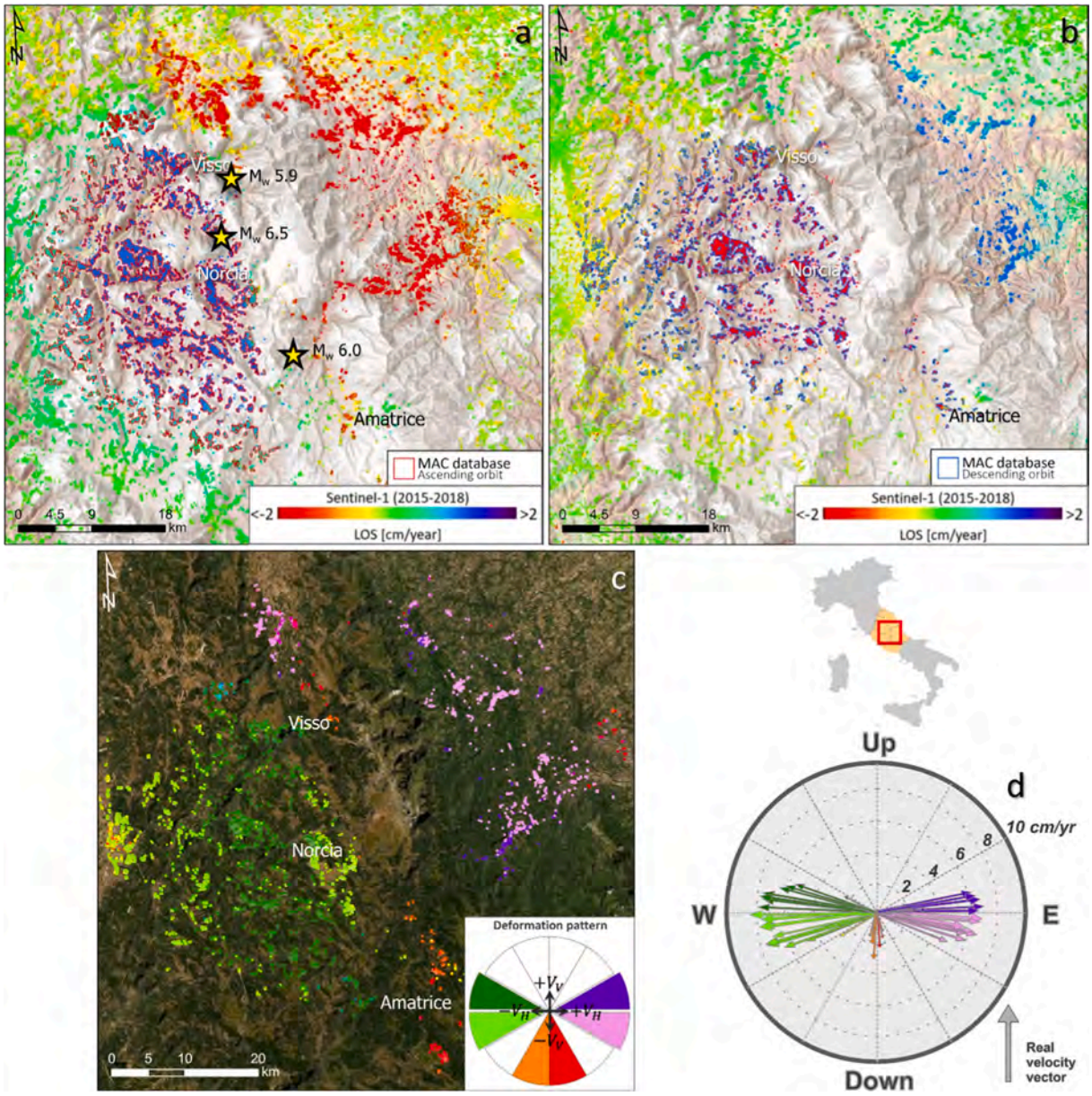

Fig. 11. 2016 Amatrice-Visso-Norcia seismic sequence results. (a, b) Ascending (a) and descending (b) deformation velocity maps of the area hit by the seismic sequence; (c) vertical and horizontal component of the deformation velocity obtained by combining LOS ascending and descending MACs; (d) polar plot depicting a representative sample of the "real" velocity vectors showing the main direction and magnitude of the observed movement. The yellow stars show the epicentres of the three mainshocks as reported by Istituto Nazionale di Geofisica e Vulcanologia (INGV) (http://arcg.is/1nfnHG). (For interpretation of the references to color in this figure legend, the reader is referred to the web version of this article.)

for the implementation of the methodology was an Intel Core i7-4790QM at 3.60 GHz, 4 cores, 8 threads, 8 MB cache, 16 GB RAM, 250 GB SSD disk and Windows 10, 64 bits. The performance testing showed that less than 21 min were needed to perform spatial clustering (Phase I of the post-processing chain) over the ascending geometry DInSAR dataset covering whole Italy (8,066,243 MPs), while it needed less than 7 min to perform the classification of the MAC ascending database (Phase II of the post-processing chain), which accounts for 8,278 polygonal clusters. Moreover, it should be pointed out that the manual preparation of the input data (*e.g.*, pre-existing inventories, ancillary information) has required additional time.

The intrinsic limit related to the interferometric analysis has influenced the outcomes of spatial clustering activities performed over DInSAR deformation maps, since the latter constitutes the main source of input. The estimation of the deformation values depends on the satellite revisiting time (impossibility to capture fast movements) and the sensor image acquisition capabilities (*i.e.*, the transmitted signal wavelength), while the possibility of detecting movements is dependent on the geometry of SAR acquisition (with respect to both the main deformation direction and the terrain topography) and the characteristics of the land cover. Indeed, only surfaces or objects that reveal a coherent signal phase within a ground pixel cell (and along time throughout all the SAR images within a data stack) lend themselves to interferometric post-processing analysis. Moreover, to obtain a 2D reconstruction of the deformation vector, the decomposition of the LOS vector into the vertical (Up-Down) and horizontal (East-West) components of deformation is needed, which is possible only if data acquired in both orbits and processed separately are available. This is indeed only possible where both ascending and descending measurements are available, further decreasing the actual scene coverage provided by the DInSAR

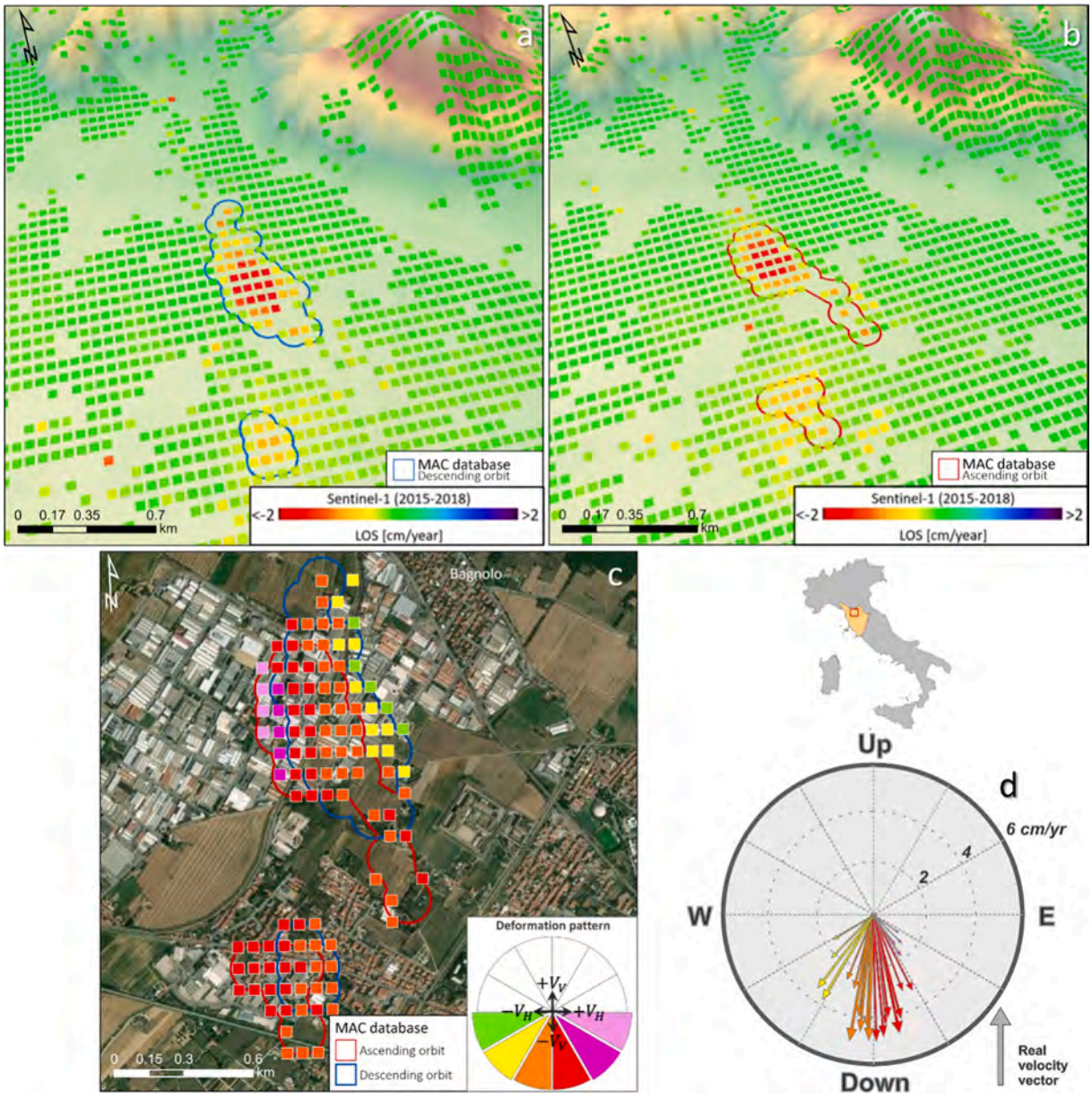

Fig. 12. Montemurlo municipality (Tuscany Region) results. (a, b) 3D view of the ascending (a) and descending (b) velocity deformation maps; (c) vertical and horizontal component of the deformation velocity obtained by combining LOS ascending and descending MACs; (d) polar plot depicting a representative sample of the "real" velocity vectors showing the main direction and magnitude of the observed movement.

measurements. All these aspects, among others, belong to a fundamental knowledge background that is necessary for a correct interpretation of DInSAR derived deformation maps.

Spatial clustering analysis, aside from suffering the same inherent limitations of interferometric techniques, strongly depends on the input parameters that are subjectively set in the semi-automatic GIS model: the estimation of both magnitude and areal extent of the observed ground deformation phenomena are tight to the setting of the displacement rate threshold, the buffer size and the minimum cluster size. Another important drawback is the classification of the underlying process which has triggered the diffuse ground deformation, thus resulting in the generation of MAC. The ancillary information and the pre-existing inventories are sometimes unavailable, incomplete, or not updated, hindering a correct pre-screening of the deforming areas. Hence, the combination of other available source of information, such as slope maps and the mean value of vertical and horizontal components of deformation, when this information is available, may become necessary (see Section 2.2.3). In particular, the lack of adequate ancillary information and the insufficient interferometric data resulted in 1,044 unclassified MAC, which corresponds to 7.1% of the total clustered areas considering both the ascending and descending database. On the other hand, a total of 8,234 out of 14,638 MAC (considering both geometries of acquisition) have been classified as potential landslides, potential subsidence or potential uplift, solely on the basis of the ratio between mean vertical and horizontal components of displacement and local slope value. In terms of number of units, either potential landslide and potential subsidence classes are two of the main representative categories within the classified MAC database (*i.e.*, 28.1% and 27.9% respectively, considering the totality of MAC), thus suggesting that many sectors of the Italian territory are suffering from ground deformation phenomena which have not still been recorded by the present inventories. The significance of the semi-automated classification method inherent with the two potential phenomena is tied to some considerations carried out on MAC classified as landslide and subsidence

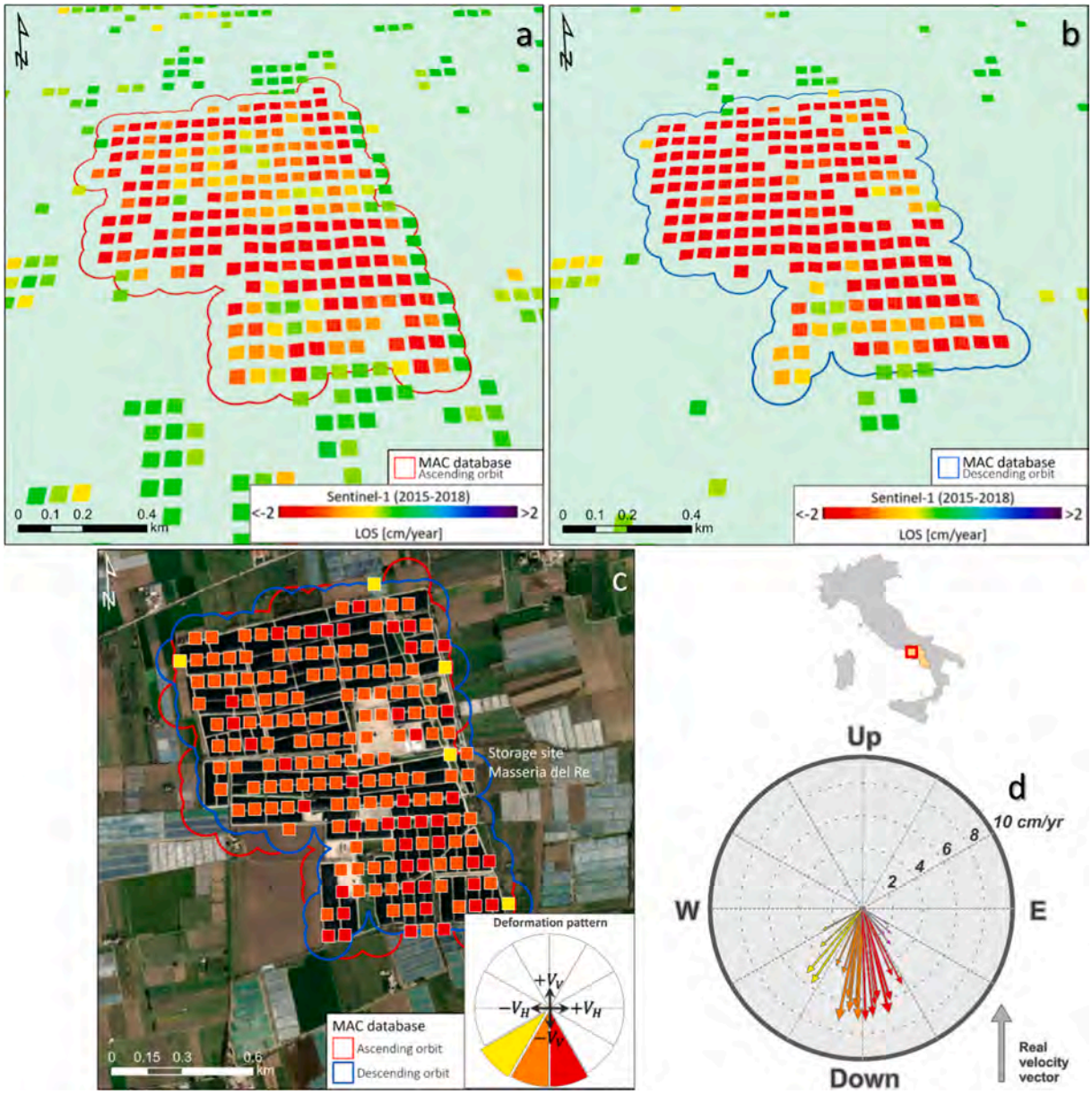

Fig. 13. Masseria del Re storage site (Campania Region) results. (a, b) 3D view of the ascending (a) and descending (b) deformation velocity maps; (c) vertical and horizontal component of the deformation velocity obtained by combining LOS ascending and descending MACs; (d) polar plot depicting a representative sample of the "real" velocity vectors showing the main direction and magnitude of the observed movement.

according to the pre-existing geohazard inventories, which therefore can be considered as "ground truth".

Considering the LOS components mean ratio values ($|V_V|/|V_H|$), the 100% of the subsidence-MAC (534 units) are associated to values greater than 1, while the landslide-MAC (2083 units) accounts for 1879 units with values less than 1 and 204 units with values greater than 1. Having also considered a 5° slope angle threshold to distinguish between landslide and subsidence events (Iwanashi et al., 2003; Lee et al., 2004), it is reported that, again, the totality of subsidence-MAC stands below that limit (average slope value less than 5°), while 2058 out of 2083 landslide-MAC stand above that limit (average slope value greater than 5°).

It is evident that the vertical component of the movement is predominant in subsidence-related moving areas, while the landslide-related ones does not show a sharp tendence in this sense. The scattered values associated to slope deformations could be ascribed to a great variability in terms of kinematic behaviours (since all type of slope movements are here considered) and to the relative spatial distribution of the MPs within each landslide, where the deformation pattern may be partially hidden to satellite sensors (Frattini et al., 2018). Despite the limitation that could arise in the pre-screening of potential landslides, it emerges the relative high confidence in correctly interpreting MAC as potential subsidence phenomena.

The presented work is, at our knowledge, the first example of semi-automated mapping and pre-assessment of the Earth surface deformations at national scale. Other approaches with a similar task have been previously applied only for local scale (Barra et al., 2017), basin scale (Bianchini et al., 2012; Lu et al., 2012) or regional scale (Meisina et al., 2008; Montalti et al., 2019; Solari et al., 2019) analysis. The presented site-specific pattern deformation analysis (*i.e.*, the third phase of the post-processing chain) constitutes an innovative scheme for data interpretation and visualization. Indeed, the colormap and the polar plot, proposed throughout the various case studies (see section 3.3), enable a more precise and comprehensive view of the magnitude and

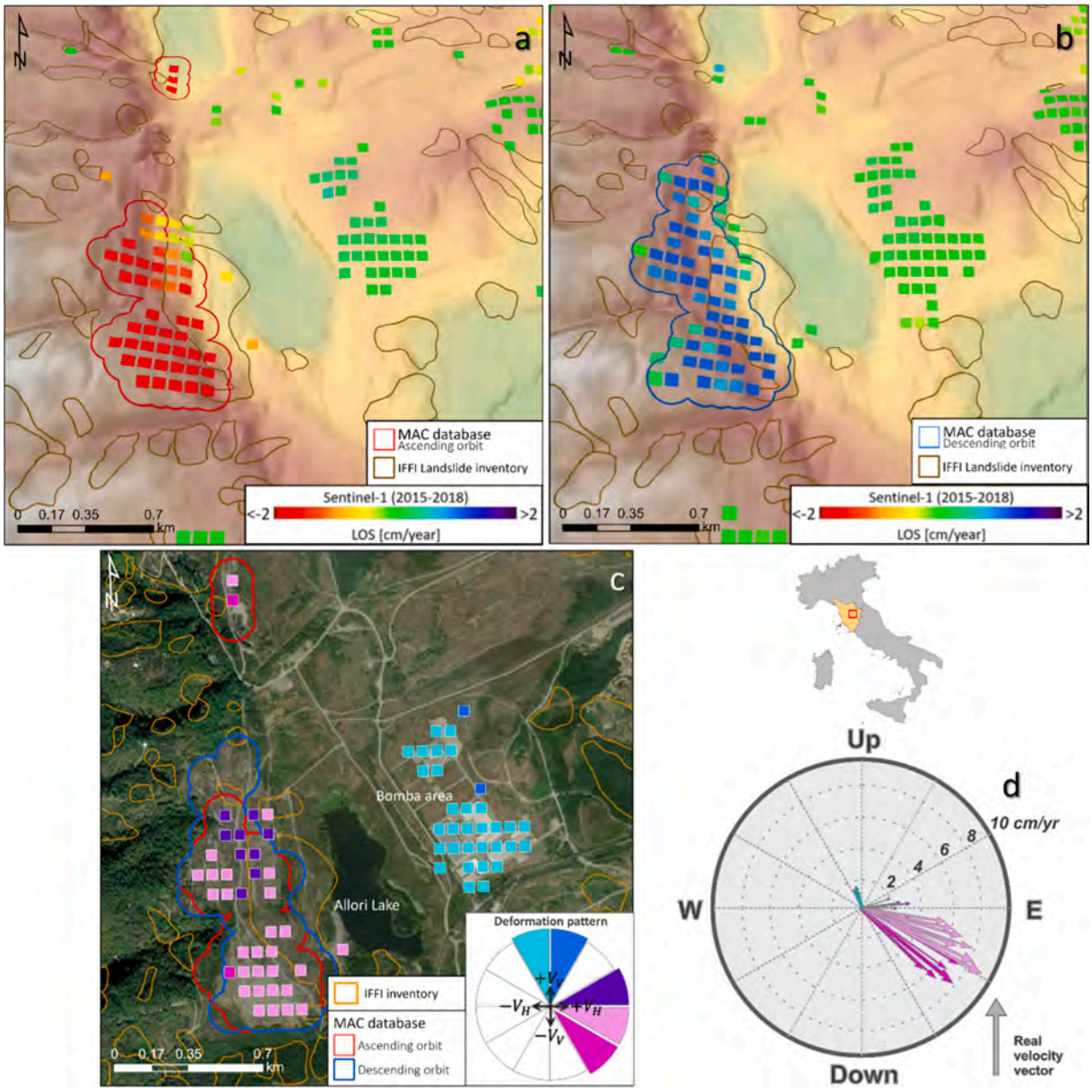

Fig. 14. Santa Barbara (Tuscany Region) results. (a, b) 3D view of the ascending (a) and descending (b) deformation velocity maps; (c) vertical and horizontal component of the deformation velocity obtained by combining LOS ascending and descending MACs; (d) polar plot depicting a representative sample of the "real" velocity vectors showing the main direction and magnitude of the observed movement.

direction of the observed motion occurred on the Up-Down and East-West plane.

Leveraging on thematic information already available, such as the landslide database compiled by Herrera et al. (2018), outputs of this mapping systems may be fully integrated along with the upcoming deliveries of continental-scale ground motion data (EGMS), as they represent the key step for the optimal management of billions of MPs, for the benefit of expert and non-expert users, for public and private scenarios. Moreover, the creation of updated databases regarding the ongoing ground deforming areas could serve for: (*i*) reference for Civil Protection purposes and policy makers devoted to territorial planning; (*ii*) prioritization of the available funds in the framework of development of new structural plans; (*iii*) updating of geohazard inventories; (*iv*) creation of more advanced products such as landslide intensity maps (Bianchini et al., 2017; Catani et al., 2005; Lu et al., 2014), given the lack of information on the expected velocities for a large number of landslides (Cigna et al., 2013); (*v*) validation data for landslide and subsidence susceptibility maps.

In the near future, more complex and refined algorithms (*e.g.*, machine learning and deep learning algorithms) will likely be exploited together with other sources of information (e.g., optical images, displacement time series) for the sake of improving precision of automatic and near-real-time ground deformation mapping and classification on the basis of continental-scale interferometric dataset. In particular, the DInSAR time series analysis may foster space time pattern mining to discern areas suffering from linear, periodical, or irregular motion trends which may be embedded in complex ground deformation phenomena, such as earthquake and volcanic affected areas, where different sources of deformation may overlap.

In the general framework of the geohazard risk reduction, it is here shown that by means of periodically delivered SAR-derived data and consequent post-processing analysis, it is nowadays possible to start filling the knowledge gap related to the ongoing hazardous surface deformations that the territory has been facing, thus constituting the first

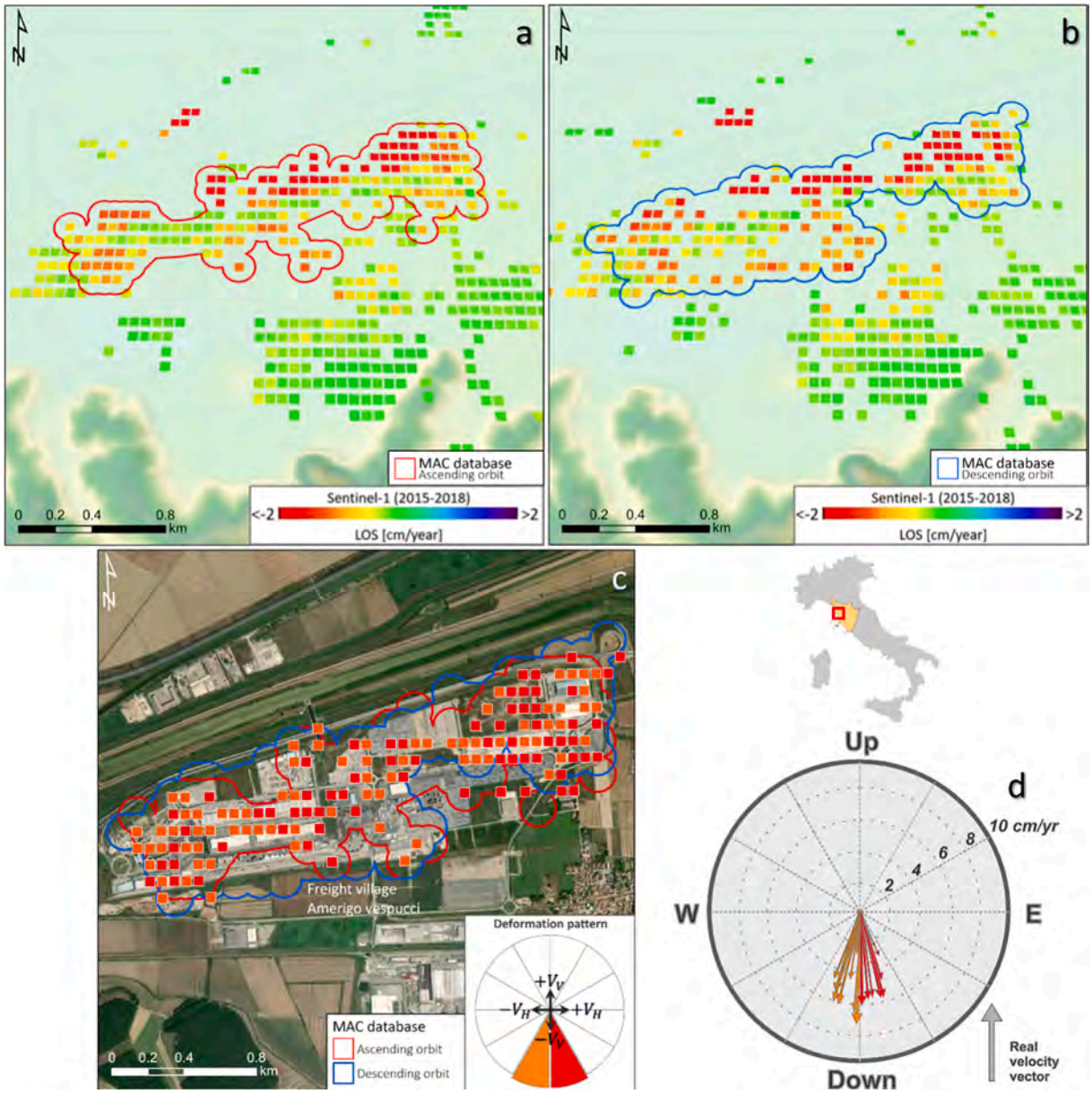

Fig. 15. Freight village Amerigo Vespucci (Tuscany Region) results. (a, b) 3D view of the ascending (a) and descending (b) deformation velocity maps; (c) vertical and horizontal component of the deformation velocity obtained by combining LOS ascending and descending MACs; (d) polar plot depicting a representative sample of the "real" velocity vectors showing the main direction and magnitude of the observed movement.

milestone on the path to an effective and comprehensive prevention and risk management.

5. Conclusions

In this work, semi-automatic spatial clustering analyses are performed on nation-wide multi-temporal DInSAR data in order to map and classify active and potential instability phenomena affecting the Italian Peninsula. The proposed approach is carried out on the P-SBAS results (ground pixel size about 80 m × 80 m) covering the whole Italian territory over both ascending and descending orbits and exploiting the whole S1 IWS archive from March 2015 – December 2018.

The analysis of the P-SBAS results has enhanced the detection of newly activated surface deformation events with a millimetric accuracy, thus demonstrating that such activities may constitute an asset for future geohazards risk management practices. In the framework of land management for civil protection purposes, the proposed methodology can be effectively used to obtain the preliminary filtering and pre-screening activity of newly updated DInSAR datasets covering very wide areas, guaranteeing fast and handy results for expert and non-expert users.

Due to intrinsic constraints of the DInSAR approach (*e.g.* the wavelength of the SAR sensor and the revisit time of the satellite above a certain target), only slow-moving deformation phenomena can be detected. Taking into consideration the above-mentioned limitations, the focus of the presented analysis is based on three main objectives: (*i*) identification and analysis of distributed MPs representative of a relatively high average displacement behavior within the Italian territory; (*ii*) aggregation of the targets in different polygonal clusters, which are intended to define newly activated phenomena in the time-span of our analysis; (*iii*) classification of the underlying natural or anthropic process which has triggered the observed surface deformation.

A total number of 14,638 MACs constituted by at least 3 neighboring MPs with a displacement threshold of ± 1 cm/year has been retrieved from both the ascending and descending DInSAR datasets which were

then pre-screened in 11 categories: earthquake-induced deformations, volcanic-related processes, landslides, potential landslides, subsidence, potential subsidence, potential uplift, dump site activities, mining activities, construction site activities and unclassified. It is necessary to state that the number and the spatial extent of the MAC are inevitably tight to the subjective settings of the GIS model parameters. Secondly, the rationale of the adopted classification procedure strongly relies on the availability of the ancillary data, on literature assumptions and on theoretical thresholds regarding the ratio between the vertical and horizontal motion components. In the near future, fully automated and data-driven approaches may be investigated for feature detection and extraction, while a confidence degree could be applied to each correctly classified deforming areas.

CRediT authorship contribution statement

Davide Festa: Conceptualization, Methodology, Investigation, Formal analysis, Writing – original draft, Data Curation, Visualization. **Manuela Bonano:** Validation, Writing - Review & Editing. **Nicola Casagli:** Supervision, Project administration. **Pierluigi Confuorto:** Data Curation, Validation. **Claudio De Luca:** Data curation, Software, Investigation, Visualization, Writing - Review & Editing. **Matteo Del Soldato:** Visualization, Data Curation. **Riccardo Lanari:** Supervision, Writing - Review & Editing, Funding acquisition. **Ping Lu:** Writing - Review & Editing. **Michele Manunta:** Validation, Writing - Review & Editing. **Mariarosaria Manzo:** Data curation, Writing - Review & Editing, Funding acquisition. **Giovanni Onorato:** Data curation, Software, Writing - Review & Editing. **Federico Raspini:** Supervision , Validation, Writing - Review & Editing. **Ivana Zinno:** Data curation, Software, Writing - Review & Editing. **Francesco Casu:** Supervision , Validation, Writing - Review & Editing, Funding acquisition, Project administration.

Declaration of Competing Interest

The authors declare the following financial interests/personal relationships which may be considered as potential competing interests: Riccardo Lanari and Nicola Casagli reports a relationship with Presidency of the Council of Ministers - Department of civil protection and Italian Ministry of Economic Development that includes: funding grants.

Acknowledgements

This research was partially funded by the “Presidenza del Consiglio dei Ministri–Dipartimento della Protezione Civile” (Presidency of the Council of Ministers–Department of Civil Protection), through the IREA-CNR/DPC and CPC-UNIFI agreements. The contents of this paper represent the authors’ ideas and do not necessarily correspond to the official opinion and policies of DPC. This paper was also partially funded by the IREA CNR/Italian Ministry of Economic Development DGS-UNMIG (now Italian Ministry of Ecologic Transition DGISSEG) 2018-2019 agreement.

References

Acocella, V., 2008. Activating and reactivating pairs of nested collapses during caldera-forming eruptions: Campi Flegrei (Italy). Geophys. Res. Lett. 35 (17) https://doi.org/10.1029/2008GL035078.

Amadei, M., Bagnaia, R., Lureti, L., Lugeri, F., Lugeri, N., Feoli, E., Dragan, M., Fernetti, M., & Oriolo, G., 2003. Il progetto CARTA DELLA NATURA alla scala 1: 250.000. Metodologia di realizzazione (in Italian).

Barra, A., Solari, L., Béjar-Pizarro, M., Monserrat, O., Bianchini, S., Herrera, G., Crosetto, M., Sarro, R., González-Alonso, E., Mateos, R., Ligüerzana, S., López, C., Moretti, S., 2017. A methodology to detect and update active deformation areas based on sentinel-1 SAR images. Remote Sens. 9 (10), 1002. https://doi.org/10.3390/rs9101002.

Berardino, P., Costantini, M., Franceschetti, G., Iodice, A., Pietranera, L., Rizzo, V., 2003. Use of differential SAR interferometry in monitoring and modelling large slope instability at Maratea (Basilicata, Italy). Eng. Geol. 68 (1-2), 31–51.

Berardino, P., Fornaro, G., Lanari, R., Sansosti, E., 2002. A new algorithm for surface deformation monitoring based on small baseline differential SAR interferograms. Geosci. Remote Sens., IEEE Trans. 40 (11), 2375–2383.

Bevilacqua, A., Neri, A., De Martino, P., Isaia, R., Novellino, A., Tramparulo, F.D.A., Vitale, S., 2020. Radial interpolation of GPS and leveling data of ground deformation in a resurgent caldera: application to Campi Flegrei (Italy). J. Geod. 94, 1–27.

Bianchini, S., Cigna, F., Righini, G., Proietti, C., Casagli, N., 2012. Landslide hotspot mapping by means of persistent scatterer interferometry. Environ. Earth Sci. 67 (4), 1155–1172.

Bianchini, S., Raspini, F., Solari, L., Del Soldato, M., Ciampalini, A., Rosi, A., Casagli, N., 2018. From Picture to Movie: Twenty Years of Ground Deformation recording over Tuscany Region (Italy) with Satellite InSAR. Front. Earth Sci. 6, 177.

Bianchini, S., Solari, L., Casagli, N., 2017. A gis-based procedure for landslide intensity evaluation and specific risk analysis supported by persistent scatterers interferometry (PSI). Remote Sens. 9 (11), 1093. https://doi.org/10.3390/rs9111093.

Bonì, R., Bordoni, M., Vivaldi, V., Troisi, C., Tararbra, M., Lanteri, L., Zucca, F., Meisina, C., 2020. Assessment of the Sentinel-1 based ground motion data feasibility for large scale landslide monitoring. Landslides 17 (10), 2287–2299.

Bonì, R., Bosino, A., Meisina, C., Novellino, A., Bateson, L., McCormack, H., 2018. A methodology to detect and characterize uplift phenomena in urban areas using Sentinel-1 data. Remote Sens. 10 (4), 607. https://doi.org/10.3390/rs10040607.

Bozzuto, P., Geroldi, C., 2021. The former mining area of Santa Barbara in Tuscany and a spatial strategy for its regeneration. The Extractive Industries Society 8 (1), 147–158.

Calò, F., Ardizzone, F., Castaldo, R., Lollino, P., Tizzani, P., Guzzetti, F., Lanari, R., Angeli, M.-G., Pontoni, F., Manunta, M., 2014. Enhanced landslide investigations through advanced DInSAR techniques: The Ivancich case study, Assisi, Italy. Remote Sens. Environ. 142, 69–82.

Casu, F., Elefante, S., Imperatore, P., Zinno, I., Manunta, M., De Luca, C., Lanari, R., 2014. SBAS-DInSAR parallel processing for deformation time-series computation. IEEE J. Selected Topics in Appl. Earth Observations Remote Sens. 7 (8), 3285–3296.

Catani, F., Casagli, N., Ermini, L., Righini, G., Menduni, G., 2005. Landslide hazard and risk mapping at catchment scale in the Arno River basin. Landslides 2 (4), 329–342.

Cheloni, D., 2017. Geodetic model of the 2016 Central Italy earthquake sequence inferred from InSAR and GPS measurements. In, *EGU General Assembly Conference Abstracts* (p. 9191).

Chiodini, G., Selva, J., Del Pezzo, E., Marsan, D., De Siena, L., D’Auria, L., Bianco, F., Caliro, S., De Martino, P., Ricciolino, P., Petrillo, Z., 2017. Clues on the origin of post-2000 earthquakes at Campi Flegrei caldera (Italy). Sci. Rep. 7 (1) https://doi.org/10.1038/s41598-017-04845-9.

Ciampalini, A., Solari, L., Giannecchini, R., Galanti, Y., Moretti, S., 2019. Evaluation of subsidence induced by long-lasting buildings load using InSAR technique and geotechnical data: The case study of a Freight Terminal (Tuscany, Italy). Int. J. Appl. Earth Observation Geoinform. 82, 101925. https://doi.org/10.1016/j.jag.2019.101925.

Cigna, F., Bianchini, S., Casagli, N., 2013. How to assess landslide activity and intensity with Persistent Scatterer Interferometry (PSI): the PSI-based matrix approach. Landslides 10 (3), 267–283.

Coda, S., Confuorto, P., De Vita, P., Di Martire, D., Allocca, V., 2019. Uplift evidences related to the recession of groundwater abstraction in a pyroclastic-alluvial aquifer of southern Italy. Geosciences 9 (5), 215. https://doi.org/10.3390/geosciences9050215.

Crosetto, M., Solari, L., Mróz, M., Balasis-Levinsen, J., Casagli, N., Frei, M., Oyen, A., Moldestad, D.A., Bateson, L., Guerrieri, L., Comerci, V., Andersen, H.S., 2020. The evolution of wide-area dinsar: From regional and national services to the European ground motion service. Remote Sens. 12 (12), 2043. https://doi.org/10.3390/rs12122043.

D’Auria, L., Pepe, S., Castaldo, R., Giudicepietro, F., Macedonio, G., Ricciolino, P., Tizzani, P., Casu, F., Lanari, R., Manzo, M., Martini, M., Sansosti, E., Zinno, I., 2015. Magma injection beneath the urban area of Naples: a new mechanism for the 2012–2013 volcanic unrest at Campi Flegrei caldera. Sci. Rep. 5 (1) https://doi.org/10.1038/srep13100.

De Luca, C., Casu, F., Manunta, M., Onorato, G., & Lanari, R., 2021. Comment on “Study of Systematic Bias in Measuring Surface Deformation With SAR Interferometry” by Ansari et al. (2021).

De Luca, C., Zinno, I., Manunta, M., Lanari, R., Casu, F., 2017. Large areas surface deformation analysis through a cloud computing P-SBAS approach for massive processing of DInSAR time series. Remote Sens. Environ. 202, 3–17.

De Novellis, V., Atzori, S., De Luca, C., Manzo, M., Valerio, E., Bonano, M., Cardaci, C., Castaldo, R., Di Bucci, D., Manunta, M., Onorato, G., Pepe, S., Solaro, G., Tizzani, P., Zinno, I., Neri, M., Lanari, R., Casu, F., 2019. DInSAR analysis and analytical modeling of Mount Etna displacements: The December 2018 volcano-tectonic crisis. Geophys. Res. Lett. 46 (11), 5817–5827.

De Zan, F., Monti Guarnieri, A., 2006. TOPSAR: Terrain observation by progressive scans. IEEE Trans. Geosci. Remote Sens. 44 (9), 2352–2360.

Dehls, J.F., Larsen, Y., Marinkovic, P., Lauknes, T.R., Stødle, D., & Moldestad, D.A., 2019. INSAR. No: A National Insar Deformation Mapping/Monitoring Service In Norway–From Concept To Operations. In, *IGARSS 2019-2019 IEEE International Geoscience and Remote Sensing Symposium* (pp. 5461-5464): IEEE.

Del Soldato, M., Solari, L., Raspini, F., Bianchini, S., Ciampalini, A., Montalti, R., Ferretti, A., Pellegrineschi, V., Casagli, N., 2019. Monitoring ground instabilities using SAR satellite data: a practical approach. ISPRS Int. J. Geo-Inf. 8 (7), 307. https://doi.org/10.3390/ijgi8070307.

Di Martire, D., Paci, M., Confuorto, P., Costabile, S., Guastaferro, F., Verta, A., Calcaterra, D., 2017. A nation-wide system for landslide mapping and risk

management in Italy: The second Not-ordinary Plan of Environmental Remote Sensing. Int. J. Appl. Earth Observ. Geoinform. 63, 143–157.
Ezquerro, P., Del Soldato, M., Solari, L., Tomás, R., Raspini, F., Ceccatelli, M., Fernández-Merodo, J., Casagli, N., Herrera, G., 2020. Vulnerability assessment of buildings due to land subsidence using InSAR data in the ancient historical city of Pistoia (Italy). Sensors 20 (10), 2749. https://doi.org/10.3390/s20102749.
Farina, P., Casagli, N., Ferretti, A., 2007. Radar-interpretation of InSAR measurements for landslide investigations in civil protection practices. First North American Landslide Conference 272–283.
Fedele, L., Insinga, D.D., Calvert, A.T., Morra, V., Perrotta, A., Scarpati, C., 2011. 40 Ar/39 Ar dating of tuff vents in the Campi Flegrei caldera (southern Italy): toward a new chronostratigraphic reconstruction of the Holocene volcanic activity. Bull. Volcanol. 73 (9), 1323–1336.
Fornaro, G., Franceschetti, G., Lanari, R., Rossi, D., Tesauro, M., 1997a. Interferometric SAR phase unwrapping using the finite element method. IEE Proceedings-Radar, Sonar Navigation 144 (5), 266. https://doi.org/10.1049/ip-rsn:19971259.
Fornaro, G., Franceschetti, G., Lanari, R., Sansosti, E., Tesauro, M., 1997b. Global and local phase-unwrapping techniques: a comparison. J. Opt. Soc. Am. 14 (10), 2702. https://doi.org/10.1364/JOSAA.14.002702.
Fortunato, C., Martino, S., Prestininzi, A., Romeo, R., 2012. New release of the Italian catalogue of earthquake-induced ground failures (CEDIT).
Frattini, P., Crosta, G.B., Rossini, M., Allievi, J., 2018. Activity and kinematic behaviour of deep-seated landslides from PS-InSAR displacement rate measurements. Landslides 15 (6), 1053–1070.
Gabriel K., A., Goldstein M, R, Zebker A, H, 1989. Mapping small elevation changes over large areas: Differential radar interferometry. J. Geophys. Res. 94 (B7), 9183–9191. https://doi.org/10.1029/JB094iB07p09183.
Herrera, G., Mateos, R.M., García-Davalillo, J.C., Grandjean, G., Poyiadji, E., Maftei, R., Filipciuc, T.-C., Jemec Auflič, M., Jež, J., Podolszki, L., Trigila, A., Iadanza, C., Raetzo, H., Kociu, A., Przyłucka, M., Kułak, M., Sheehy, M., Pellicer, X.M., McKeown, C., Ryan, G., Kopačková, V., Frei, M., Kuhn, D., Hermanns, R.L., Koulermou, N., Smith, C.A., Engdahl, M., Buxó, P., Gonzalez, M., Dashwood, C., Reeves, H., Cigna, F., Liščák, P., Pauditš, P., Mikulėnas, V., Demir, V., Raha, M., Quental, L., Sandić, C., Fusi, B., Jensen, O.A., 2018. Landslide databases in the Geological Surveys of Europe. Landslides 15 (2), 359–379.
Huang, M.H., Fielding, E.J., Liang, C., Milillo, P., Bekaert, D., Dreger, D., Salzer, J., 2017. Coseismic deformation and triggered landslides of the 2016 Mw 6.2 Amatrice earthquake in Italy. Geophys. Res. Lett. 44, 1266–1274.
Improta, L., Latorre, D., Margheriti, L., Nardi, A., Marchetti, A., Lombardi, A.M., Castello, B., Villani, F., Ciaccio, M.G., Mele, F.M., Moretti, M., 2019. Multi-segment rupture of the 2016 Amatrice-Visso-Norcia seismic sequence (central Italy) constrained by the first high-quality catalog of Early Aftershocks. Sci. Rep. 9 (1) https://doi.org/10.1038/s41598-019-43393-2.
Iwahashi, J., Watanabe, S., Furuya, T., 2003. Mean slope-angle frequency distribution and size frequency distribution of landslide masses in Higashikubiki area, Japan. Geomorphology 50 (4), 349–364.
Kalia, A.C., Frei, M., Lege, T., 2017. A Copernicus downstream-service for the nationwide monitoring of surface displacements in Germany. Remote Sens. Environ. 202, 234–249.
Kalia, A., 2018. Classification of landslide activity on a regional scale using persistent scatterer interferometry at the moselle valley (Germany). Remote Sens. 10 (12), 1880. https://doi.org/10.3390/rs10121880.
Kobayashi, T., Morishita, Y., Yarai, H., 2015. Detailed crustal deformation and fault rupture of the 2015 Gorkha earthquake, Nepal, revealed from ScanSAR-based interferograms of ALOS-2. Earth Planets Space 67, 1–13.
Kobayashi, T., Tobita, M., Koarai, M., Okatani, T., Suzuki, A., Noguchi, Y., Yamanaka, M., Miyahara, B., 2012. InSAR-derived crustal deformation and fault models of normal faulting earthquake (M j 7.0) in the Fukushima-Hamadori area. Earth Planets Space 64, 1209–1221.
Lanari, R., Bonano, M., Casu, F., Luca, C.D., Manunta, M., Manzo, M., Onorato, G., Zinno, I., 2020. Automatic generation of sentinel-1 continental scale DInSAR deformation time series through an extended P-SBAS processing pipeline in a cloud computing environment. Remote Sens. 12 (18), 2961. https://doi.org/10.3390/rs12182961.
Lanari, R., De Natale, G., Berardino, P., Sansosti, E., Ricciardi, G.P., Borgstrom, S., Capuano, P., Pingue, F., Troise, C., 2002. Evidence for a peculiar style of ground deformation inferred at Vesuvius volcano. Geophys. Res. Lett. 29 (9), 6-1–6-4.
Lanari, R., Mora, O., Manunta, M., Mallorqui, J.J., Berardino, P., Sansosti, E., 2004. A small-baseline approach for investigating deformations on full-resolution differential SAR interferograms. IEEE Trans. Geosci. Remote Sens. 42 (7), 1377–1386.
Lee, S., Ryu, J.-H., Won, J.-S., Park, H.-J., 2004. Determination and application of the weights for landslide susceptibility mapping using an artificial neural network. Eng. Geol. 71 (3-4), 289–302.
Lu, P., Casagli, N., Catani, F., Tofani, V., 2012. Persistent Scatterers Interferometry Hotspot and Cluster Analysis (PSI-HCA) for detection of extremely slow-moving landslides. Int. J. Remote Sens. 33 (2), 466–489.
Lu, P., Catani, F., Tofani, V., Casagli, N., 2014. Quantitative hazard and risk assessment for slow-moving landslides from Persistent Scatterer Interferometry. Landslides 11 (4), 685–696.
Lundgren, P., Rosen, P.A., 2003. Source model for the 2001 flank eruption of Mt. Etna volcano. Geophys. Res. Lett. 30.
Manconi, A., Walter, T.R., Manzo, M., Zeni, G., Tizzani, P., Sansosti, E., Lanari, R., 2010. On the effects of 3-D mechanical heterogeneities at Campi Flegrei caldera, southern Italy. J. Geophys. Res. Solid Earth 115 (B8). https://doi.org/10.1029/2009JB007099.
Manunta, M., De Luca, C., Zinno, I., Casu, F., Manzo, M., Bonano, M., Fusco, A., Pepe, A., Onorato, G., Berardino, P., De Martino, P., Lanari, R., 2019. The parallel SBAS approach for Sentinel-1 interferometric wide swath deformation time-series generation: algorithm description and products quality assessment. IEEE Trans. Geosci. Remote Sens. 57 (9), 6259–6281.
Manzo, M., Lanari, R., Antoncecchi, I., Solaro, G., Bonano, M., Buonanno, S., Castaldo, R., Casu, F., Ciccone, F., De Luca, C., 2019. Ground deformation analysis of the Italian Peninsula through space-borne SAR interferometry and geophysical modelling: the IREA-CNR/MiSE-DGS-UNMIG agreement. Geophysical Research Abstracts.
Manzo, M., Ricciardi, G.P., Casu, F., Ventura, G., Zeni, G., Borgström, S., Berardino, P., Del Gaudio, C., Lanari, R., 2006. Surface deformation analysis in the Ischia Island (Italy) based on spaceborne radar interferometry. J. Volcanol. Geoth. Res. 151 (4), 399–416.
Martino, S., 2017. Earthquake-induced landslides in Italy: from the distribution of effects to the hazard mapping. Italian J. Eng. Geol. Environ. 1, 53–67.
Massonnet, D., Rossi, M., Carmona, C., Adragna, F., Peltzer, G., Feigl, K., Rabaute, T., 1993. The displacement field of the Landers earthquake mapped by radar interferometry. Nature 364 (6433), 138–142.
Matano, F., 2019. Analysis and classification of natural and human-induced ground deformations at regional scale (Campania, Italy) detected by satellite synthetic-aperture radar interferometry archive datasets. Remote Sens. 11 (23), 2822. https://doi.org/10.3390/rs11232822.
Meisina, C., Zucca, F., Notti, D., Colombo, A., Cucchi, A., Savio, G., Giannico, C., Bianchi, M., 2008. Geological interpretation of PSInSAR data at regional scale. Sensors 8 (11), 7469–7492.
Montalti, R., Solari, L., Bianchini, S., Del Soldato, M., Raspini, F., Casagli, N., 2019. A Sentinel-1-based clustering analysis for geo-hazards mitigation at regional scale: a case study in Central Italy. Geomatics, Natural Hazards Risk 10 (1), 2257–2275.
Morishita, Y.u., Lazecky, M., Wright, T., Weiss, J., Elliott, J., Hooper, A., 2020. LiCSBAS: an open-source InSAR time series analysis package integrated with the LiCSAR automated Sentinel-1 InSAR processor. Remote Sens. 12 (3), 424. https://doi.org/10.3390/rs12030424.
Notti, D., Herrera, G., Bianchini, S., Meisina, C., García-Davalillo, J.C., Zucca, F., 2014. A methodology for improving landslide PSI data analysis. Int. J. Remote Sens. 35 (6), 2186–2214.
Osmanoğlu, B., Dixon, T.H., Wdowinski, S., Cabral-Cano, E., Jiang, Y., 2011. Mexico City subsidence observed with persistent scatterer InSAR. Int. J. Appl. Earth Observation Geoinform. 13 (1), 1–12.
Patra, A., Bevilacqua, A., Pitman, E.B., Bursik, M., Voight, B., Neri, A., Flandoli, F., De Martino, P., Giudicepietro, F., & Macedonio, G., 2019. A statistical approach for spatial mapping and temporal forecasts of volcanic eruptions using monitoring data. In, AGU 2019 Fall Meeting.
Pepe, A., Lanari, R., 2006. On the extension of the minimum cost flow algorithm for phase unwrapping of multitemporal differential SAR interferograms. IEEE Trans. Geosci. Remote Sens. 44 (9), 2374–2383.
Pepe, A., Yang, Y., Manzo, M., Lanari, R., 2015. Improved EMCF-SBAS processing chain based on advanced techniques for the noise-filtering and selection of small baseline multi-look DInSAR interferograms. IEEE Trans. Geosci. Remote Sens. 53 (8), 4394–4417.
Rizzo, V., 2002. GPS monitoring and new data on slope movements in the Maratea Valley (Potenza, Basilicata). Phys. Chem. Earth, Parts A/B/C 27 (36), 1535–1544.
Rizzo, V., & Limongi, P., 1997. Risultati inclinometrici ed indagini geologico-stratigrafiche nel Centro Storico di Maratea (Lucania, Italia). *Geografia Fisica e Dinamica Quaternaria, 20*, 137-144 (in Italian).
Rosi, A., Tofani, V., Tanteri, L., Stefanelli, C.T., Agostini, A., Catani, F., Casagli, N., 2017. The new landslide inventory of Tuscany (Italy) updated with PS-InSAR: geomorphological features and landslide distribution. Landslides 1–15.
Solari, L., Del Soldato, M., Bianchini, S., Ciampalini, A., Ezquerro, P., Montalti, R., Raspini, F., Moretti, S., 2018. From ERS 1/2 to Sentinel-1: subsidence monitoring in Italy in the last two decades. Front. Earth Sci. 6, 149.
Solari, L., Del Soldato, M., Montalti, R., Bianchini, S., Raspini, F., Thuegaz, P., Bertolo, D., Tofani, V., Casagli, N., 2019. A Sentinel-1 based hot-spot analysis: landslide mapping in north-western Italy. Int. J. Remote Sens. 40 (20), 7898–7921.
Solari, L., Del Soldato, M., Raspini, F., Barra, A., Bianchini, S., Confuorto, P., Casagli, N., Crosetto, M., 2020. Review of satellite interferometry for landslide detection in Italy. Remote Sens. 12 (8), 1351. https://doi.org/10.3390/rs12081351.
Tarquini, S., Vinci, S., Favalli, M., Doumaz, F., Fornaciai, A., Nannipieri, L., 2012. Release of a 10-m-resolution DEM for the Italian territory: Comparison with global-coverage DEMs and anaglyph-mode exploration via the web. Comput. Geosci. 38 (1), 168–170.
Tizzani, P., Castaldo, R., Solaro, G., Pepe, S., Bonano, M., Casu, F., Manunta, M., Manzo, M., Pepe, A., Samsonov, S., Lanari, R., Sansosti, E., 2013. New insights into the 2012 Emilia (Italy) seismic sequence through advanced numerical modeling of ground deformation InSAR measurements. Geophys. Res. Lett. 40 (10), 1971–1977.
Tomás, R., Pagán, J.I., Navarro, J.A., Cano, M., Pastor, J.L., Riquelme, A., Cuevas-González, M., Crosetto, M., Barra, A., Monserrat, O., J.M., L.-S., A., R., S., I., M., D.S., L., S., S., B., F., R., F., N., A., F., M., C., F., T., G., H., & N., C., 2019. Semi-automatic identification and pre-screening of geological–geotechnical deformational processes using persistent scatterer interferometry datasets. Remote Sens., 11, 1675.
Torres, R., Snoeij, P., Geudtner, D., Bibby, D., Davidson, M., Attema, E., Potin, P., Rommen, BjÖrn, Floury, N., Brown, M., Traver, I.N., Deghaye, P., Duesmann, B., Rosich, B., Miranda, N., Bruno, C., L'Abbate, M., Croci, R., Pietropaolo, A., Huchler, M., Rostan, F., 2012. GMES Sentinel-1 mission. Remote Sens. Environ. 120, 9–24.

Zhao, J., Konietzky, H., 2020. Numerical analysis and prediction of ground surface movement induced by coal mining and subsequent groundwater flooding. Int. J. Coal Geol. 229, 103565. https://doi.org/10.1016/j.coal.2020.103565.

Zinno, I., Bonano, M., Buonanno, S., Casu, F., De Luca, C., Manunta, M., Manzo, M., Lanari, R., 2020. National scale surface deformation time series generation through advanced DInSAR processing of sentinel-1 data within a cloud computing environment. IEEE Trans. Big Data 6 (3), 558–571.

Zinno, I., Elefante, S., Mossucca, L., De Luca, C., Manunta, M., Terzo, O., Lanari, R., Casu, F., 2015. A first assessment of the P-SBAS DInSAR algorithm performances within a cloud computing environment. IEEE J. Selected Topics in Appl. Earth Observ. Remote Sens. 8 (10), 4675–4686.

Geoportale Difesa del Suolo. https://geoportale.lamma.rete.toscana.it/difesa_suolo/#/ (accessed 5 August 2021).

Map of the Amatrice-Visso-Norcia seismic sequence. http://arcg.is/1nfnHG (accessed 5 August 2021).

Osservatorio Vesuviano 2018, "Bollettino di sorveglianza Campi Flegrei – dicembre 2018". https://www.ov.ingv.it/ov/bollettini-mensili-campania/Bollettino_Mensile_Campi_Flegrei_2018_12.pdf (accessed 5 August 2021).

Osservatorio Vesuviano 2021, "Bollettino di sorveglianza Campi Flegrei – dicembre 2021". https://www.ov.ingv.it/ov/bollettini-mensili-campania/Bollettino Mensile_Campi_Flegrei_2021_06.pdf (accessed 5 August 2021).